PAPER

Check for updates

Bio-based antimicrobial nanocomposites derived from tannery waste for functional leather coating: circular valorization of chrome shaving dust

Sharmin Akter Liza,[a] Md. Abdulla-Al-Mamun, [iD] *[a] Md. Nazmul Islam,[a] Md. Rezaul Karim Rana[b] and Md. Shariful Islam[c]

This study aimed to establish a waste valorization approach by developing bio-based antimicrobial nanocomposites and exploring their potential reuse within a circular economy framework. Protein was extracted from chrome-tanned shaving dust through eco-friendly microbial degradation using *Bacillus thuringiensis* SRL4A. Four types of metal–protein-based nanocomposites, namely protein–ZnO, Ag–protein, polyaniline (PANI)/protein–ZnO, and PANI/Ag–protein, were synthesized using the protein hydrolysate derived from tannery solid waste and incorporated into leather finishing formulations. Characterization techniques, including TKN, amino acid analysis, SDS-PAGE, UV-vis spectroscopy, FT-IR, XRD, zeta potential analysis, TGA, SEM, and EDX, were employed to determine the functional groups, crystallographic structure, thermal stability, morphology, and composition of the nanocomposites. TKN analysis confirmed that the protein content in the sample obtained from shaving dust was 73.08% and other analyses confirmed the successful incorporation of metal particles into the protein matrix. The particle sizes of the synthesized nanocomposites were 32 nm (protein–ZnO), 34 nm (Ag–protein), 44 nm (PANI/protein–ZnO), and 45 nm (PANI/Ag–protein). Cytotoxicity tests revealed that all nanocomposites were non-toxic to living cells. The minimum inhibitory concentration (MIC) values for protein–ZnO were 0.325 mg mL^{-1} against Gram-positive *B. cereus* and 1.25 mg mL^{-1} against Gram-negative *E. coli*. For Ag–protein, PANI/protein–ZnO, and PANI/Ag–protein, the MIC was 0.625 mg mL^{-1} against both *B. cereus* and *E. coli*. All nanocomposites exhibited antimicrobial activity, with protein–ZnO showing the highest zone of inhibition (ZOI = 20 mm) against *B. cereus* and Ag–protein showing the highest ZOI (22 mm) against *E. coli*. Leather samples coated with varying amounts of nanocomposites in different finishing formulations demonstrated effective antibacterial activity and met the standard requirements for finish film quality and mechanical performance. Notably, protein–ZnO-treated leather exhibited the highest ZOI (18 mm) against *B. cereus*, while Ag–protein-treated leather achieved the highest ZOI (14 mm) against *E. coli*. This work presents a sustainable approach to repurposing tannery waste into high-performance antimicrobial materials, with potential applications in the leather, textile, packaging, and biomedical industries, as well as the valorization of protein derived from tannery waste.

1. Introduction

In recent years, bio-nanocomposites have attracted considerable attention owing to their eco-friendly nature and diverse potential applications across various fields.[1] These hybrid materials comprise both inorganic or organic nanoparticles (NPs) and bio-based polymers, with the nanoparticles typically exhibiting at least one dimension on the nanometre scale.[2] Among these, metal–protein-based nanocomposites have emerged as promising candidates. Proteins possess several advantageous characteristics, such as biocompatibility, flexibility, abundant availability, biodegradability, and multiple reactive sites, often referred to as 'cavities', that make them ideal building blocks for high-performance nanocomposites.[3]

During nanocomposite synthesis, proteins are commonly employed as capping agents that function as stabilizers, limiting nanoparticles' overgrowth and preventing their aggregation or coagulation. Capping ligands play a crucial role in maintaining the stability of the interface between nanoparticles and

[a] *Institute of Leather Engineering and Technology, University of Dhaka, 44-50 Hazaribagh, Dhaka-1209, Bangladesh. E-mail: mamun.ilet@du.ac.bd*

[b] *Molecular Biology Laboratory, Department of Biochemistry and Molecular Biology, Faculty of Biological Sciences, University of Dhaka, Dhaka 1000, Bangladesh*

[c] *Department of Veterinary and Animal Sciences, University of Rajshahi, Rajshahi-6205, Bangladesh*

their synthesis medium.[4] Due to their amphiphilic nature, capping agents impart functionality and enhance compatibility with other phases, facilitating improved integration within nanocomposite systems.[5] Proteins utilize their polar head groups to coordinate with metal atoms, while their non-polar tails interact with the surrounding medium. This amphiphilic nature makes proteins highly effective as capping agents in the synthesis of nanocomposites. Metal–protein nanocomposites exhibit a versatile range of properties, including high mechanical strength,[6] bio-degradability, thermal stability, and light barrier capabilities.[7,8] Additionally, they demonstrate vapor permeability, surface adhesion, and notable antifungal and antibacterial activities.[9]

Among the various promising applications of nanocomposites, antibacterial functionality stands out as one of the most compelling. Their ability to disrupt microbial activity through mechanisms such as physical interaction, oxidative stress induction, and controlled release of antimicrobial agents makes them powerful candidates for integration into medical devices, packaging materials, and environmental systems.[10,11] The structural versatility and tunable surface properties of nanocomposites further enhance their efficacy in targeting a wide range of pathogenic microorganisms.[12,13]

Leather finishing represents a pivotal stage in the leather manufacturing process, wherein raw hides undergo surface treatments to acquire enhanced durability, aesthetic appeal, and functional performance. This phase is instrumental in imparting key properties such as hydrophobicity, colour fastness, rub resistance, gloss, and uniform texture to the final product.[14] Conventional finishing formulations typically employ film-forming agents based on proteins, such as casein, or synthetic resins like polyurethanes and polyacrylates. Protein-based systems, particularly those utilizing casein, offer a natural appearance and thermostability, though they may exhibit limitations in water resistance and rub fastness.[15] In contrast, resin-based formulations provide superior mechanical strength, abrasion resistance, and chemical stability, making them widely adopted in industrial leather finishing applications.[16]

The leather finishing process traditionally involves the use of environmentally detrimental substances, including volatile organic compounds (VOCs), non-biodegradable resins, and potentially hazardous cross-linking agents, all of which aim to enhance the physical and mechanical properties of leather.[14] These chemical inputs contribute significantly to air pollution and pose serious risks to both environmental integrity and occupational health. In response to these challenges, various strategies have been proposed, most of which centre on the use of cross-linking agents to improve film-forming capabilities. However, to align with contemporary sustainability goals, it is imperative to further innovate leather finishing technologies by improving product performance while reducing reliance on harmful chemicals. This includes the advancement of bio-nanocomposite-based finishing systems that integrate highly compatible base and top coats. Despite the critical importance of this finishing phase, limited progress has been made in developing formulations that utilize proteins derived from industry-generated waste. Recent research has explored the synergistic application of such protein-based materials with nanotechnology, offering a promising pathway toward circular and eco-conscious leather manufacturing.[14,17,18]

Previous studies have reported the utilization of various biopolymers in nanocomposite formulations, including egg albumen,[19,20] fish skin gelatin,[21] fenugreek and mung bean proteins,[22] corn silk extract,[23] chitosan,[24] soy protein,[25] and whey protein.[26] All these systems, metal atoms such as aluminum, lead, silver, gold, iron, cobalt, zinc, cadmium, titanium, and copper, have been incorporated to enhance functional properties.[27] More recently, polyaniline (PANI)-functionalized metal nanocomposites have gained attention due to PANI's high electrical conductivity, environmental stability, facile synthesis, and notable antibacterial and antifungal activities.[20] The polymer exhibits multiple oxidation states, and its physicochemical properties, including color, conductivity, and antimicrobial efficacy, are influenced by its oxidation and protonation levels.

In parallel, to mitigate microbial contamination on leather surfaces resulting from prolonged human contact, several nanocomposite-based treatments have been developed to impart antifungal and antibacterial characteristics. Notable examples include Ag–NiO$_2$ composites,[28] polyacrylate–ZnO nanocomposites,[29] TiO$_2$–polyacrylate emulsions,[30] and casein–ZnO hybrid systems.[31]

In this study, a protein hydrolysate derived from tannery shaving dust – a significant solid waste stream containing approximately 15–30% proteinaceous material – was employed as a capping agent for the synthesis of metal–protein nanocomposites.[32] Tannery shaving dust predominantly comprises chromium-cross-linked collagen, a by-product of leather processing that is typically discarded through environmentally detrimental practices such as open burning or landfilling. These disposal methods contribute to soil and air pollution, raising serious ecological concerns.

To the best of our knowledge, this is the first report detailing the utilization of protein extracted from such waste for the fabrication of nanocomposites, including protein–ZnO, Ag–protein, PANI/protein–ZnO, and PANI/Ag–protein systems. The protein hydrolysate was obtained *via* microbial degradation, a bio-based approach that facilitates the breakdown of complex collagen structures into functional peptides suitable for nanomaterial synthesis. Zinc and silver were selected as the metal components due to their well-documented antibacterial efficacy and compatibility with protein matrices.

The resulting nanocomposites were subsequently integrated into leather coating formulations to evaluate their potential as sustainable and antimicrobial alternatives in tannery finishing processes. This approach not only valorizes industrial waste but also aligns with circular economy principles by transforming hazardous residues into value-added functional materials.

2. Materials and methods

2.1. Chemicals and materials

All reagents used in this study were of analytical grade, except for those employed in leather finishing, which were of

industrial grade. Zinc sulfate ($ZnSO_4 \cdot 7H_2O$), silver nitrate ($AgNO_3$), sodium borohydride ($NaBH_4$), ammonium persulfate ((NH_4)$_2S_2O_8$), ferric chloride ($FeCl_3$), and ethanol (C_2H_5OH) were procured from Sigma-Aldrich and Merck Chemical Groups. Purified sodium hydroxide (NaOH) pellets, magnesium oxide (MgO), and hydrochloric acid (HCl, 37%) were obtained from Active Fine Chemicals Ltd, Dhaka, Bangladesh. Nutrient broth and Mueller–Hinton agar media were sourced from HiMedia Laboratories Pvt. Ltd, India. Leather finishing chemicals, including pigment, isopropyl alcohol (IPA), acrylic resin, polyurethane (PU), protein binder/lustre, compact binder, nitrocellulose (NC) lacquer, and silicon, were supplied by Stahl, Germany. The Institute of Leather Engineering and Technology, University of Dhaka, provided goat crust leather.

2.2. Extraction of the protein hydrolysate from tannery shaving dust

Shaving dust collected from a tannery was dried at 100 °C for 30 min. Distilled water (10 mL g^{-1} of chrome shavings) and tryptone (12% w/w) were added, followed by sterilization *via* autoclaving. After cooling to 50–60 °C, a bacterial cell suspension of *Bacillus thuringiensis* SRL4A (PP802975) at 35% v/w was inoculated. The mixture was incubated for 100 h at 150 rpm in a rotary shaker. Post-incubation, the hydrolysate was centrifuged at 10 000 rpm for 20 min, filtered, and treated with MgO and NaOH at 55 °C for 2 h to precipitate chromium as insoluble $Cr(OH)_3$.[33] Throughout this study, the resulting dechromed protein hydrolysate is referred to as "protein". The protein was subjected to various characterization analyses, including determination of the final chromium content in the protein sample. The process and result of the analyses are reported in our previous paper.[33]

2.3. Synthesis of nanocomposites

2.3.1. Protein–ZnO nanocomposite synthesis.
A volume of 5 mL of protein hydrolysate was mixed with 20 mL of deionized water (DI) containing 1.0 M $ZnSO_4 \cdot 7H_2O$ and stirred until fully dissolved. The pH of the solution was adjusted using 2 M NaOH, followed by sonication for 10 min to ensure homogeneous mixing. The mixture was incubated in a rotary shaker for 12 h, after which white precipitates were observed. These precipitates were separated by centrifugation and washed thoroughly with ethanol and DI water to remove residual impurities. The resulting nanocomposite was dried at 200 °C for 2 h and ground into a fine powder (Fig. 1a).

2.3.2. Ag–protein nanocomposite synthesis.
A 1.0 M solution of $AgNO_3$ was prepared by dissolving 1.0 g of $AgNO_3$ in 15 mL of deionized (DI) water, and the mixture was thoroughly mixed using a magnetic stirrer (Fisher Scientific). Subsequently, 5 mL of protein hydrolysate was added and stirred to obtain a homogeneous solution. Freshly prepared $NaBH_4$ (the molar ratio of $AgNO_3 : NaBH_4 = 1 : 2$) was dissolved in 6 mL of DI water. While the $AgNO_3$–protein hydrolysate solution was stirred vigorously, the $NaBH_4$ solution was added dropwise. Upon the addition of $NaBH_4$, the solution's colour

Fig. 1 Dried nanocomposites: (a) protein–ZnO, (b) Ag–protein, and (c) PANI/metal–protein nanocomposite.

changed from pale yellow to deep brown, accompanied by the formation of microbubbles on the surface. To ensure complete homogenization, the mixture was sonicated for 10 min, resulting in a brownish-red solution with minimal residual bubbling. The final product was collected by centrifugation, and the Ag–protein nanocomposite was obtained *via* freeze-drying of the precipitate (Fig. 1b).

2.3.3. PANI/protein–ZnO and PANI/Ag–protein nanocomposite synthesis.
A mixture containing 1 mL of aniline and 3.6 wt% of either protein–ZnO (for PANI/protein–ZnO) or Ag–protein (for PANI/Ag–protein) was dissolved in 10 mL of HCl (prepared in 100 mL of distilled water). The solution was stirred at 50 °C for 30 min, followed by the addition of 2.40 g of ammonium persulfate ((NH_4)$_2S_2O_8$) and 1.88 g of ferric chloride ($FeCl_3$). Stirring was continued for an additional 3 h to complete the polymerization. The resulting mixture was then evaporated overnight in an oven. The solid product was filtered, washed sequentially with ethanol and deionized water, and re-dried at 50 °C; the color of both composites, PANI/ZnO–protein and PANI/Ag–protein, is dark green (Fig. 1c).[34]

2.4. Finishing leather with the nanocomposites

The finishing formulations applied to upper leather are detailed in Tables 1 and 2. Four leather specimens were sprayed twice with the seasonal coat formulations, first incorporating nanocomposites and subsequently without nanocomposites, using a spray gun. The coated specimens were dried in a heater at 40 °C and then pressed at 70 kg cm^{-2} at 80 °C. Following this, a single layer of top coat formulation was applied to each specimen using one coat (two cross sprays), dried again at 40 °C, and pressed at 80 kg cm^{-2} at 80 °C. An additional leather specimen was finished using a conventional formulation, also prepared according to Tables 1 and 2. All chemical quantities are expressed in parts by weight.

Table 1 Season coat formulation

Ingredients	Conventional (1 layer)	Experimental (2 layers)
Pigment	30	—
IPA	30	24
Acrylic resin	100	—
PU	60	—
Protein binder/lustre	100	476
Compact binder	30	—
Water	650	495
Nanocomposites	—	5

Table 2 Top coat formulation

Ingredients	Conventional (1 layer)	Experimental (1 layer)
NC lacquer	645	645
Silicon	30	30
Water	325	325

2.5. Characterization techniques

2.5.1. Total Kjeldahl nitrogen (TKN) and amino acid analysis of protein. The total nitrogen content of the sample was determined using a Behr–Labor Behrotest nitrogen analyzer (Model K20L), following the standard Kjeldahl method as described elsewhere.[35] This method involves digestion, distillation, and titration steps to quantify nitrogen present in organic compounds. The measured nitrogen content was then converted to total protein content by applying a nitrogen-to-protein conversion factor of 6.25, which is commonly used for proteinaceous materials. The total protein content was calculated using the following equation:

$$\text{Total Kjeldahl Nitrogen(TKN)}$$
$$= \frac{(\text{mL HCl sample} - \text{mL HCl blank}) \times N \text{ of HCl} \times 14.007 \times 100}{1000 \times \text{weight of the sample (mg)}}$$

$$(1)$$

Amino acid profiling of the samples was conducted in accordance with AOAC Official Method 982.30, designated for the analysis of amino acids in foods and feeds.[36] The analysis was performed using a Sykam Amino Acid Analyzer (Model S433; Sykam GmbH, Germany), which operates on ion-exchange chromatography coupled with post-column ninhydrin derivatization for quantification.

For sample preparation, 0.20–1.00 g of a finely powdered sample was hydrolyzed with 6 M hydrochloric acid (HCl) containing 0.1% (w/v) phenol to prevent oxidative degradation of tyrosine. The acid hydrolysis was carried out in sealed glass ampoules at 110 °C for 24 hours. Upon completion of hydrolysis, the reaction mixture was cooled to room temperature, and the pH was carefully adjusted to the range of 2.9–3.1 using a sodium hydroxide (NaOH) solution to ensure compatibility with the chromatographic system.

The resulting hydrolysate was filtered through a 0.25 μm syringe filter to remove particulates and transferred to the autosampler vials. Quantification of individual amino acids was achieved by comparing the retention times and peak areas of the sample chromatograms with those of authenticated amino acid standards analyzed under identical conditions.

2.5.2. UV-visible and Fourier transform infrared (FTIR) spectroscopy. The optical properties of the samples were investigated using UV-visible spectroscopy. Measurements were conducted with a T60 UV-visible spectrophotometer (PG Instruments Ltd, England) across the wavelength range of 200–800 nm. This analysis provided insights into the electronic transitions and absorbance behavior of the materials, which are indicative of their structural and compositional attributes.

Fourier-transform infrared (FTIR) spectroscopy was employed to identify the presence of specific functional groups and to monitor alterations in the secondary structure of the samples. The spectra were recorded using a Bruker ALPHA II FT-IR spectrometer (Bruker Optik GmbH, Germany) within the wavenumber range of 4000–500 cm^{-1}, at a spectral resolution of 4 cm^{-1}. This technique enabled the detection of characteristic vibrational modes associated with molecular bonds, thereby facilitating a detailed understanding of the chemical interactions and structural modifications occurring within the material matrix.

2.5.3. X-ray diffraction, ζ potential and thermogravimetric analysis (TGA). X-ray powder diffraction (XRD) analysis was performed to investigate the crystalline structure and phase composition of the composite's samples. The diffraction patterns were recorded using a Rigaku Miniflex II desktop diffractometer (Rigaku Corporation, Japan) over a 2θ range of 10° to 80°, operating in fixed-time mode with a scanning rate of 4° min^{-1} at ambient temperature. This technique enabled the identification of characteristic diffraction peaks, providing insights into the degree of crystallinity and lattice parameters of the material.

Surface charge properties were assessed through zeta potential (ζ-potential) measurements using a zeta potential instrument (Malvern Panalytical Ltd., UK). Prior to analysis, the samples were sonicated to ensure uniform dispersion and subsequently injected into a 100 μL measurement cell. The instrument determined the electrophoretic mobility of the particles, which was then used to calculate the ζ-potential, offering valuable information regarding colloidal stability and surface interactions.

The thermal stability and decomposition behavior of the samples were evaluated using thermogravimetric analysis (TGA), conducted on a TGA 8000 thermogravimetric analyzer (PerkinElmer Inc., USA). Approximately 5 mg of each sample was placed in a platinum crucible mounted on the microbalance pan. The samples were heated from 50 °C to 700 °C at a constant rate of 10 °C min^{-1} under a nitrogen atmosphere maintained at a flow rate of 20 mL min^{-1}. The resulting thermograms provided quantitative data on weight loss events, enabling interpretation of thermal degradation stages and compositional stability.

2.5.4. Field emission scanning electron Microscopy (FE-SEM) and energy dispersive X-ray (EDX) spectroscopy analysis. The morphological features of the prepared samples were examined using a Field Emission Scanning Electron Microscope (FESEM, model JSM-7610F, JEOL Ltd, Japan), which offers high-resolution imaging suitable for nanoscale surface analysis. Prior to imaging, the specimens were carefully mounted onto aluminum stubs using carbon conductive adhesive tape to ensure optimal electrical conductivity and minimize charging effects during scanning. To further enhance surface conductivity and image clarity, the samples were sputter-coated with a thin layer of gold using a vacuum coating unit.

In conjunction with FESEM analysis, elemental composition and distribution were assessed using an integrated Energy-Dispersive X-ray (EDX) spectroscopy system. This technique

enabled qualitative and semi-quantitative identification of the constituent elements present in the sample matrix, thereby complementing the morphological observations with compositional insights.

2.5.5 SDS-PAGE analysis of the dechromed hydrolysate and nanocomposite. The molecular weight distribution of the dechromed hydrolysate was analyzed using sodium dodecyl sulfate polyacrylamide gel electrophoresis (SDS-PAGE). Samples (10 mg mL^{-1}) were mixed with Laemmli sample buffer, heat-denatured at 70 °C, and loaded onto a 12% polyacrylamide separating gel. Electrophoresis was performed at 100 V for 20 min during the stacking phase, followed by 150 V for 50 min to separate proteins (Bio-Rad, USA). After electrophoresis, the gel was fixed in 50% methanol and 10% acetic acid for 60 min, stained with Coomassie Brilliant Blue for 60 min, and then destained using 40% methanol and 10% acetic acid for 60 min, followed by overnight destaining in distilled water.

2.6. Antibacterial evaluation of the nanocomposite and nanocomposite-coated leather

2.6.1. Cytotoxicity assessment test. Cytotoxicity analysis was performed to evaluate the potential toxicological effects of the nanocomposite samples on mammalian cells. Vero cells, derived from the kidney epithelial tissue of the African green monkey (*Cercopithecus aethiops*), were selected as the *in vitro* model due to their sensitivity and widespread use in toxicity screening. The cells were cultured in Dulbecco's Modified Eagle's Medium (DMEM), supplemented with 10% fetal bovine serum (FBS) to support cell growth and proliferation, along with 1% penicillin–streptomycin (1 : 1) and 0.2% gentamycin to prevent microbial contamination.

A cell suspension containing 1.5×10^4 cells per 100 μL was seeded into sterile 96-well microplates and incubated at 37 °C in a humidified atmosphere containing 5% CO_2 to allow for cell attachment and stabilization. After 24 hours of incubation, 25 μL of the autoclaved nanocomposite sample was introduced into each well. The treated cells were further incubated for 48 hours under the same conditions.

Cytotoxic effects were evaluated using an inverted light microscope by observing morphological changes, including cell shrinkage, detachment, and loss of membrane integrity. All treatments were performed in duplicate to ensure reproducibility and statistical reliability.

2.6.2. Minimum inhibitory concentration (MIC) of the nanocomposites. The antibacterial efficacy of the synthesized nanocomposites was evaluated using the standard broth dilution method, following the Clinical and Laboratory Standards Institute (CLSI) guidelines (M07-A8). This method enables the determination of the minimum inhibitory concentration (MIC) by assessing visible microbial growth in liquid media. Nanocomposite samples were serially diluted in twofold increments using sterile nutrient broth, yielding final concentrations ranging from 5.00 mg mL^{-1} to 0.156 mg mL^{-1}. For each dilution, 0.1 mL of bacterial inoculum, comprising *Bacillus cereus* and *Escherichia coli* at a concentration of 1×10^6 CFU mL^{-1}, standardized to 0.5 McFarland, was added to the test tubes.

To ensure accurate interpretation, two control tubes were included: one containing only the bacterial suspension in nutrient broth (positive control), and the other containing uninoculated nutrient broth (negative control). All tubes were incubated at 37 °C for 18 hours under aerobic conditions. The MIC was defined as the lowest concentration of the nanocomposite at which no visible turbidity was observed, indicating complete inhibition of bacterial growth. Visual assessments of turbidity were recorded both prior to and following incubation to confirm MIC values, in accordance with established protocols.[37]

2.6.3. Antimicrobial efficiency assay. The antimicrobial efficacy of the synthesized nanocomposites was evaluated against two representative bacterial strains: *Bacillus cereus* (a Gram-positive bacterium) and *Escherichia coli* (a Gram-negative bacterium). The agar well diffusion method was employed to evaluate the inhibitory potential of the nanocomposite formulations, while a modified disk diffusion approach was used to assess the antimicrobial activity of nanocomposite-coated leather samples.

For the agar well diffusion assay, Mueller–Hinton agar plates were uniformly inoculated with bacterial suspensions standardized to 1×10^6 CFU mL^{-1} (0.5 McFarland standard) using sterile cotton swabs to ensure even distribution across the agar surface. Wells of 6 mm diameter were aseptically punched into the agar using a sterile cork borer. Each well was carefully loaded with 50 μL of the nanocomposite sample, which had been previously sterilized under ultraviolet (UV) light for 15 minutes to eliminate potential contaminants. Care was taken to dispense the sample slowly to prevent overflow and ensure consistent diffusion. The inoculated plates were incubated at 37 °C for 24 hours under aerobic conditions. Following incubation, the diameter of the zone of inhibition (ZOI) was measured in millimeters using a sterile ruler, and the results were recorded to quantify antimicrobial activity.

In parallel, the antimicrobial performance of nanocomposite-coated leather was evaluated using a modified disk diffusion protocol. A leather specimen (5 mm diameter) was sterilized under UV light for 15 minutes and placed directly onto the inoculated agar surface, ensuring that the finished film side was in contact with the medium. The plates were incubated under identical conditions (37 °C for 24 hours), and the ZOI surrounding the leather samples was measured to determine the extent of bacterial inhibition.

2.7. Mechanical tests of coated leather

Prior to testing, all leather specimens were conditioned under standardized laboratory conditions at a temperature of 23 ± 2 °C and a relative humidity of 65 ± 3%, in accordance with ISO 2419 guidelines, for 48 hours. Subsequent performance assessments were conducted using established SATRA methodologies to evaluate mechanical durability, thermal resistance, water vapor permeability, and adhesive bond strength. The SATRA TM-08 protocol was employed to assess surface damage and colour transfer under both dry and wet abrasion conditions. In the dry rub fastness test, a cotton felt pad was rotated over the leather surface under a 2.5 kg load, simulating mechanical

wear. For wet rub fastness, the same procedure was performed without any applied load, with the felt pre-moistened to replicate exposure to moisture. Post-abrasion, the extent of colour change and staining on both the leather sample and the cotton felt was evaluated using the ISO 105-A02 grey scale for colour change and ISO 105-A03 for staining, providing a semi-quantitative measure of fastness performance. Thermal resistance was determined using the SATRA TM-49 method, which evaluates the visible effects of brief contact between the leather surface and a heated metal block. The test identifies changes such as discoloration, shrinkage, burning, melting, or smearing. Each specimen was graded using the ISO 105-A02 grey scale, allowing for standardized comparison of thermal degradation across samples. Water vapor transmission characteristics were measured according to SATRA TM-172, a method designed to assess breathability in leathers and textiles intended for footwear and apparel applications. Each leather specimen was affixed to a test pot containing desiccant-grade silica gel and exposed to controlled air conditions for 16 hours. The water vapor permeability (WVP) was calculated based on the mass change of the silica gel using the following equation:

$$\text{Water vapor permeability} = \frac{M_2 - M_1}{A(T_2 - T_1)} \text{mg cm}^{-2} \text{ h}^{-1} \quad (2)$$

Bond strength was evaluated through a custom adhesion test. Epoxy resin was uniformly applied to a pre-conditioned leather strip, which was then bonded to a rigid plastic plate. The assembly was air-dried for 30 minutes, followed by compression under a 2 kg load for 24 hours to ensure uniform adhesion. The bonded specimen was subsequently subjected to incremental loading until detachment occurred. The maximum load at failure was recorded, providing a quantitative measure of adhesive integrity between the leather and polymer substrate.

3. Results and discussion

3.1. Characteristic analysis of proteins and composites

3.1.1. Protein and amino acid determination in shaving dust. The Kjeldahl method was employed as a representative and widely accepted analytical technique for quantifying nitrogen. Using eqn (1), the Total Kjeldahl Nitrogen (TKN) content of the shaving dust sample was determined to be 11.69%. Following nitrogen quantification, the crude protein content was calculated by applying a standard conversion factor of 6.25, yielding a total protein value of 73.08%. This conversion factor is derived from the assumption that proteins typically contain approximately 16% nitrogen and that all nitrogen present in the sample is protein-bound, as established in the previous literature.[38] The resulting protein percentage reflects the nitrogen-to-protein transformation inherent to the Kjeldahl approach and underscores the high protein content of the shaving dust material analyzed.

The amino acid composition of collagen derived from the shaving dust sample is presented in Table S1 of the supplementary information. Biochemically, collagen is characterized by a distinctive repeating tripeptide sequence (Gly–X–Y), in which glycine occupies every third residue. Consequently, glycine constitutes approximately one-third of the total amino acid content in collagen.[39] In alignment with this structural motif, our analysis revealed glycine as the most abundant amino acid, with a concentration of 134.83 mg g^{-1}. The next most prevalent residues were proline (PRO) and its hydroxylated derivative hydroxyproline (HYP), which frequently occupy the X and Y positions in the collagen sequence. These amino acids are critical biochemical markers for estimating total collagen content due to their structural role in stabilizing the triple helix. In our study, the combined concentration of proline and hydroxyproline was 97.13 mg g^{-1}, reflecting the collagen-rich nature of the sample and corroborating previously reported values. In addition to these dominant residues, glutamic acid and alanine were also detected in appreciable quantities, with concentrations of approximately 60 mg g^{-1} and 57 mg g^{-1}, respectively. These findings further support the characteristic amino acid profile of collagen and are consistent with the established literature. Moreover, the final chromium content in the dechromed protein hydrolysate was also found to be 1.40 ± 0.37 ppm.

3.1.2. UV-vis absorption spectral analysis of composites. UV-visible absorption spectroscopy is a widely utilized technique for analyzing the optical properties of nanoparticles, particularly through the observation of surface plasmon resonance (SPR). SPR arises when incident electromagnetic radiation induces collective oscillations of free electrons at the nanoparticle surface. The position and intensity of SPR peaks are highly sensitive to several factors, including particle size, shape, interparticle spacing, and the dielectric properties of the surrounding medium.[40] Typically, smaller nanoparticles exhibit SPR peaks at shorter wavelengths, while larger or more asymmetrical particles display red-shifted SPR peaks at longer wavelengths.[41]

Fig. S1 in the supporting information presents the UV-vis absorption spectra of all synthesized samples. The protein–ZnO nanocomposite exhibited a distinct SPR absorption peak at approximately 355 nm, corresponding to a band gap of 3.49 eV. This value exceeds the typical band gap of bulk ZnO (∼3.3 eV), indicating a quantum confinement effect and confirming the nanoscale dimensions of the ZnO particles.[42] The protein solution alone showed a characteristic absorption peak at 280 nm, attributed to aromatic amino acid residues. This peak was also observed for the protein–ZnO nanocomposite, suggesting successful incorporation of protein within the composite matrix.

An asymmetric tail on the higher wavelength side of the SPR peak was noted, likely due to light scattering effects caused by the inhomogeneous distribution of nanocrystalline ZnO particles, which are insoluble in aqueous media.[43] Such scattering phenomena are more pronounced in larger metallic nanoparticles, such as silver, which exhibit broadened and red-shifted SPR peaks due to enhanced scattering and aggregation tendencies.

In the silver–protein nanocomposite, a prominent SPR band was observed at 405 nm, characteristic of silver nanoparticles.

The absence of peaks in the 335–560 nm range suggests that no significant aggregation occurred during synthesis.[44] The sharp and intense nature of the SPR peak further implies a high yield of well-dispersed nanoparticles.

The PANI/Ag–protein nanocomposite displayed a strong absorption peak at 411 nm, along with a broad rising absorption near 800 nm. The peak at 411 nm is attributed to the SPR of silver and ZnO nanoparticles embedded within the polyaniline (PANI) matrix and is overlapped by the polaronic transition of PANI, which occurs at a similar wavelength.[45] The broad absorption at higher wavelengths, accompanied by a free carrier tail, confirms the presence of the conducting emeraldine salt (ES) phase of PANI,[46] indicating successful polymerization and integration of the nanocomposite components.

3.1.3. FT-IR characterization of composites. Fourier-transform infrared (FTIR) spectroscopy was employed to investigate the functional groups and molecular interactions present in the synthesized nanocomposites. The FTIR spectra of all samples are presented in Fig. 2. Among the most prominent vibrational bands in protein-based materials are the amide I and amide II bands, which are indicative of the protein backbone structure.[47] The amide I band, typically observed in the range of 1700–1600 cm^{-1}, is particularly informative for assessing secondary structural elements, as it primarily arises from the C=O stretching vibrations of peptide linkages, contributing approximately 80% of the signal. In the FTIR spectrum of pure protein hydrolysate (Fig. 2a), a broad absorption band at 3290 cm^{-1} was observed, corresponding to the O–H stretching vibrations. Additionally, characteristic peaks at 1631 cm^{-1}, 1548 cm^{-1}, and 1240 cm^{-1} were assigned to amide I, amide II, and amide III bands, respectively. Peaks at 1448 cm^{-1} and 1082 cm^{-1} were attributed to C–H deformation and C–O stretching, consistent with the functional groups present in collagen.[48]

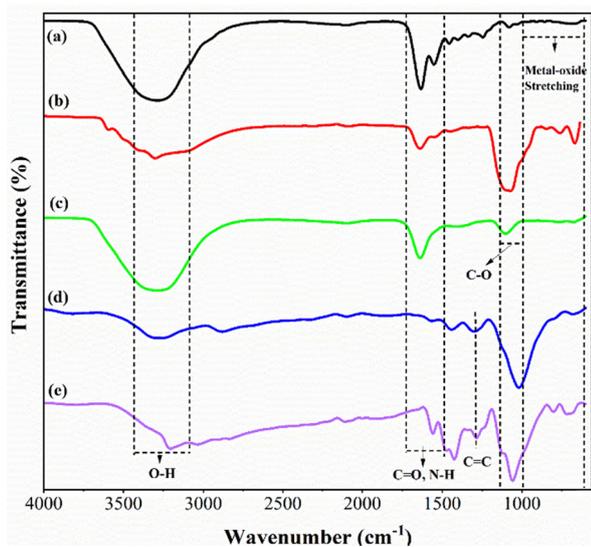The FTIR spectra of protein–ZnO and Ag–protein nanocomposites (Fig. 2b and c) showed absorption bands at positions nearly identical to those of the pure protein hydrolysate, indicating the retention of protein structural motifs. Notably, the intensification and broadening of these bands suggest the formation of a composite, likely due to protein deprotonation during nanoparticle incorporation.[49] Key absorption bands included 3290 cm^{-1} (N–H stretching), 1631 cm^{-1} (C=O stretching from –CO–NH– groups), and 576 cm^{-1} and 1082 cm^{-1}, which correspond to metal-oxide stretching vibrations, consistent with literature reports.[50]

In the Ag–protein nanocomposite, a noticeable change in the intensity of the amide I band at 1631 cm^{-1} was observed, along with modifications in other vibrational bands compared to the pure protein hydrolysate. These spectral changes may be attributed to the formation of polypeptides and amino acids during hydrolysis, which act as stabilizing agents by coating the silver nanoparticles through interactions with their functional groups.[51,52]

The FTIR spectra of PANI/protein–ZnO and PANI/Ag–protein nanocomposites (Fig. 2d and e) revealed characteristic bands at 3292, 1560, 1431, 1300, 1124, 806, and 661 cm^{-1}, resembling those of the pure protein hydrolysate, thereby confirming composite formation. The band at 3292 cm^{-1} corresponds to N–H stretching vibrations (both symmetric and asymmetric) of polyaniline (PANI). Peaks at 1560 cm^{-1} were assigned to quinoid and benzenoid ring stretching modes, while the band near 1240 cm^{-1} is associated with the quinic unit, indicative of PANI protonation. Distinctive peaks of pure PANI at 1286 cm^{-1} and 1478 cm^{-1} correspond to C=C stretching vibrations of benzenoid and quinonoid rings, respectively. Additionally, an out-of-plane C–H bending vibration at 806 cm^{-1} was observed, characteristic of p-substituted benzene rings, and a C–C stretching peak at 1124 cm^{-1} was also detected. These findings are consistent with previous reports,[53,54] further validating the successful incorporation of PANI and protein into the nanocomposite matrix.

3.1.4. X-ray diffraction (XRD) characterization of composites. X-ray diffraction (XRD) analysis was conducted to investigate the phase structure and crystallinity of the synthesized nanocomposites. The XRD patterns of all samples are presented in Fig. 3. Fig. 3a shows the XRD pattern of the protein–ZnO nanocomposite, where distinct diffraction peaks were observed at approximately 30°, 33°, 35°, and 56°, corresponding to the (100), (002), (101), and (110) crystallographic planes of hexagonal wurtzite ZnO, as indexed by JCPDS card No. 36-1451.[55] The broadening of these peaks indicates the presence of nanometer-scale crystallites, consistent with the formation of ZnO nanoparticles. The XRD pattern of the Ag–protein nanocomposite (Fig. 3b) revealed well-defined peaks at 37°, 45°, 56°, and 76°, which correspond to the (111), (200), (240), and (220) planes of face-centered cubic (FCC) silver crystals, as referenced by JCPDS file No. 06-0480. In addition to these characteristic peaks, a few unassigned reflections (marked with asterisks) were observed, suggesting the crystallization of bio-organic phases on the surface of silver nanoparticles. Similar observations have been reported in previous studies,[56,57] supporting the hybrid nature of the composite.
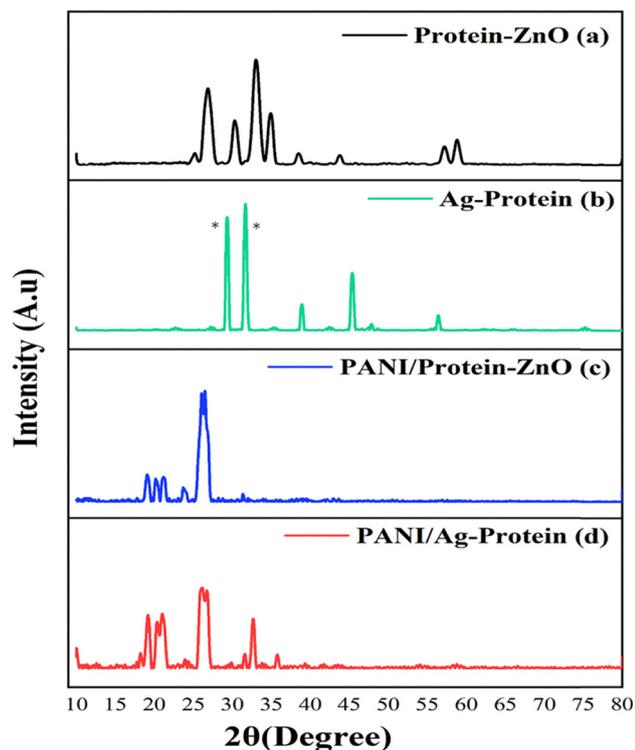

Fig. 2 FT-IR spectra of (a) protein, (b) protein–ZnO, (c) Ag–protein, (d) PANI/protein–ZnO, and (e) PANI/Ag–protein.

Fig. 3 XRD patterns of prepared (a) protein–ZnO, (b) Ag–protein, (c) PANI/protein–ZnO and (d) PANI/Ag–protein nanocomposites.

Fig. 3c and d present the XRD patterns of PANI/protein–ZnO and PANI/Ag–protein nanocomposites, respectively. Both spectra exhibit a semi-crystalline nature, characterized by two broad peaks at low diffraction angles, centered around 20° and 26°, corresponding to the (020) and (200) planes. These reflections are typically associated with periodicity parallel and perpendicular to the polymer backbone, and their sharpness and intensity reflect the degree of chain alignment and crystallite population within the polymer matrix.[58,59] In the present study, the lack of sharpness in these peaks indicates poor orientation of PANI chains, likely due to the incorporation of inorganic nanoparticles and protein components.

In the PANI/Ag–protein nanocomposite, additional peaks at 37° and 45° confirm the presence of silver nanoparticles, and their retention within the polymer matrix suggests successful incorporation and stabilization of silver within the PANI framework. Conversely, the XRD pattern of PANI/protein–ZnO revealed a reduction in ZnO crystallinity compared to the pure ZnO phase, indicating that the amorphous nature of PANI may inhibit ZnO crystal growth.[60] Nonetheless, characteristic ZnO diffraction peaks were still discernible at 30°, 32°, and 35°, confirming the presence of ZnO nanoparticles within the composite. The slight displacement of ZnO peaks in the ternary PANI/protein–ZnO nanocomposite suggests strong interfacial interactions between ZnO and the PANI matrix. Moreover, several weaker ZnO reflections were absent, likely due to the amorphous influence of polyaniline, which can suppress the crystallinity of embedded inorganic phases.[61] These findings

collectively affirm the formation of hybrid nanocomposites with distinct structural characteristics governed by the interplay between organic and inorganic components.

3.1.5. TGA and DTG analyses of nanocomposites. The thermogravimetric (TGA) and derivative thermogravimetric (DTG) profiles of all synthesized samples are presented in Fig. 4a and b, respectively. Each sample exhibited a multi-step thermal decomposition pattern, indicative of the complex structural composition and interactions among the constituent materials.

The initial weight loss observed across all samples occurred below 150 °C and is attributed to the evaporation of residual moisture and loosely bound water molecules within the matrix. The second decomposition stage, typically occurring between 200 and 350 °C, corresponds to the degradation of peptide linkages within the protein backbone. In the case of PANI/protein–ZnO and PANI/Ag–protein composites, this stage also encompasses the elimination of the acid dopant (HCl)
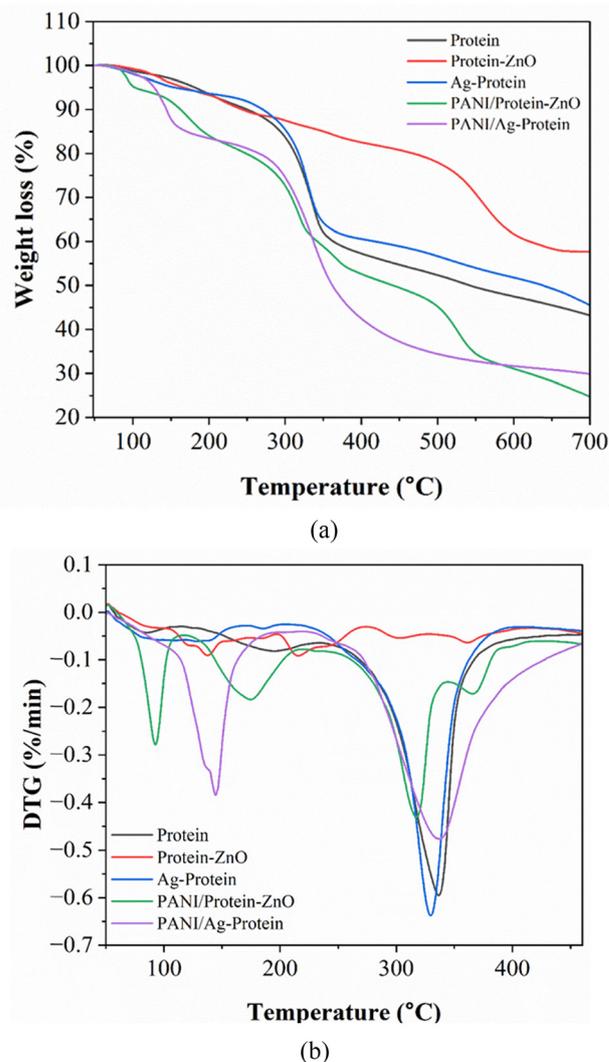

(a)

(b)

Fig. 4 (a) TGA and (b) DTG curves of protein and the prepared nanocomposites.

and low-molecular-weight oligomers of aniline from the polyaniline (PANI) backbone, as previously reported.[62,63] Additionally, the decomposition of protein-derived peptide bonds may contribute to this phase.

The third major weight loss, occurring at higher temperatures (above 400 °C), is primarily associated with the breakdown of the polymeric matrix and the thermal degradation of carbonaceous residues. This stage also involves the decomposition of inorganic constituents such as ZnO and Ag nanoparticles, as well as other thermally labile compounds embedded within the matrix.[64,65] Furthermore, the release of structural water and the cleavage of hydroxyl groups initially bound to the PANI matrix may contribute to the final degradation phase.

Among all the tested samples, the protein–ZnO composite exhibited the highest thermal stability, followed sequentially by Ag–protein, pure protein, PANI/protein–ZnO, and Ag–protein–PANI. This trend suggests that the incorporation of ZnO nanoparticles enhances the thermal resistance of the protein matrix more effectively than Ag nanoparticles or PANI-based modifications.

3.1.6. FE-SEM micrographs and EDX analysis of composites.

The morphological characteristics of the synthesized nanocomposites were examined using field emission scanning electron microscopy (FESEM), as illustrated in Fig. 5(a1–d1). Fig. 7a1 presents the FESEM image of the protein–ZnO nanocomposite, revealing nanoparticles with predominantly spherical morphology, interspersed with hexagonal and cubic shapes. This observation aligns with previous reports indicating that ZnO nanoparticles tend to exhibit spherical geometry at lower precursor concentrations, while higher concentrations yield a mixture of spherical, hexagonal, and cubical forms.[66,67] The surface of the protein–ZnO nanocomposite appears smooth and well-defined, with minimal aggregation, suggesting that the protein matrix effectively functions as a stabilizing agent during nanoparticle formation.

In Fig. 5b1, the Ag–protein nanocomposite displays small, spherical silver nanoparticles (AgNPs) uniformly dispersed within the protein matrix, indicating successful encapsulation and stabilization. Fig. 5c1 depicts the integration of ZnO nanoparticles within the rod-like structure of polyaniline (PANI), forming the PANI/protein–ZnO composite. The FESEM image of PANI/Ag–protein (Fig. 5d1) reveals that the AgNPs, exhibiting a somewhat spherical morphology, are homogeneously dispersed throughout the PANI polymer matrix. Additionally, agglomerated fibrous structures are evident on the surfaces of both PANI/protein–ZnO and PANI/Ag–protein composites, as shown in the supplementary figures (Fig. S2a and b), indicating partial clustering of polymer chains and embedded nanoparticles.

The particle size distribution for each nanocomposite was analyzed by fitting the histogram data to a log-normal distribution function, as illustrated in Fig. 5(a2–d2). The calculated average particle sizes were found to be 32 nm for protein–ZnO, 34 nm for Ag–protein, 44 nm for PANI/protein–ZnO, and 45 nm for PANI/Ag–protein, respectively. These values reflect the

influence of polymeric encapsulation and nanoparticle loading on particle growth and dispersion.

To further confirm the elemental composition and assess the chemical purity of the nanocomposites, energy dispersive X-ray (EDX) spectroscopy analysis was performed (Fig. S3). The EDX spectra verified the presence of key elements expected in the formulations. Signals corresponding to carbon, nitrogen, and oxygen were consistent with the protein matrix, while the detection of silver and zinc confirmed the successful incorporation of AgNPs and ZnO nanoparticles. The elemental profiles obtained from EDX analysis are in agreement with the theoretical composition of the respective nanocomposites, thereby validating the synthesis approach and material integrity.

3.1.7. Molecular weight distribution of the dechromed hydrolysate.

SDS-PAGE analysis of the dechromed hydrolysate revealed no distinct protein bands across the gel (Fig. S5). Instead, a smeared pattern was observed in sample S-5 (protein hydrolysate), suggesting the presence of heterogeneous, low-molecular-weight peptide fragments rather than intact proteins. This confirms extensive hydrolysis of the original protein material and supports the suitability of the peptide-rich hydrolysate for effective capping and stabilization during nanoparticle synthesis.

3.1.8. ζ-Potential analysis of nanocomposites.

Zeta potential is a critical parameter in the characterization of colloidal systems, particularly nanocomposites, as it reflects the electrostatic potential at the shear plane of dispersed particles. Nanocomposites, which consist of a polymeric matrix embedded with nanoscale fillers such as nanoparticles or nanotubes, rely on stable colloidal dispersion for optimal performance and functionality. The magnitude and sign of the zeta potential provide insight into the stability of these dispersions. Particles exhibiting high absolute zeta potential values, typically greater than +30 mV or less than −30 mV, are considered electrostatically stabilized due to strong interparticle repulsion, which prevents aggregation and flocculation. Conversely, particles with zeta potential values within the range of −10 mV to +10 mV are regarded as nearly neutral and prone to instability due to insufficient repulsive forces.[68]

Fig. 6 illustrates the zeta potential profiles of the synthesized nanocomposites across varying pH conditions. The protein–ZnO nanocomposite exhibited zeta potential values ranging from +4.1 mV to 13.6 mV, with the highest value observed at pH 8. The Ag–protein nanocomposite demonstrated a broader range, from +6 mV to −31.7 mV at pH 10, indicating enhanced colloidal stability under alkaline conditions. Similarly, the PANI/protein–ZnO and PANI/Ag–protein composites showed zeta potential ranges of +5 mV to −27 mV and +5 mV to −27.6 mV, respectively. These variations suggest that the surface charge of the nanocomposites is highly pH-dependent, with near-neutral values under acidic and neutral conditions and increasingly negative values under basic conditions.

The predominance of negative zeta potential values across the nanocomposites implies improved colloidal stability, reduced aggregation tendency, and enhanced biocompatibility. Such characteristics are particularly advantageous for biomedical

applications, including bone tissue engineering, where negatively charged surfaces have been shown to promote cell viability and integration.[69] Furthermore, the tunable surface charge behavior of these nanocomposites underscores their versatility in diverse physiological environments, supporting their potential use in targeted delivery systems and implantable biomaterials.
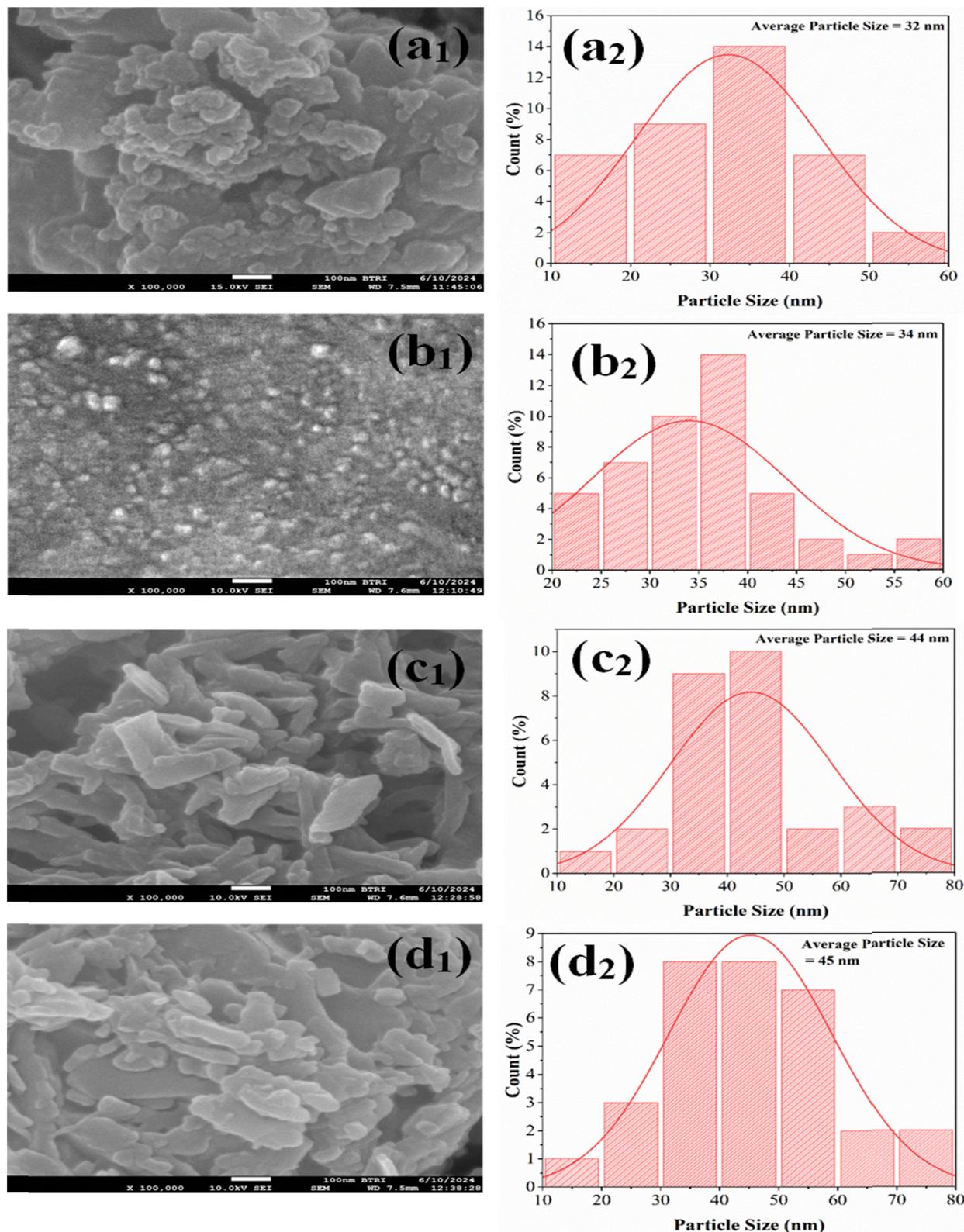

Fig. 5 SEM analysis of (a) protein–ZnO (a_1 and a_2), (b) Ag–protein (b_1 and b_2), (c) PANI/protein–ZnO (c_1 and c_2) and (d) PANI/Ag–protein (d_1 and d_2).
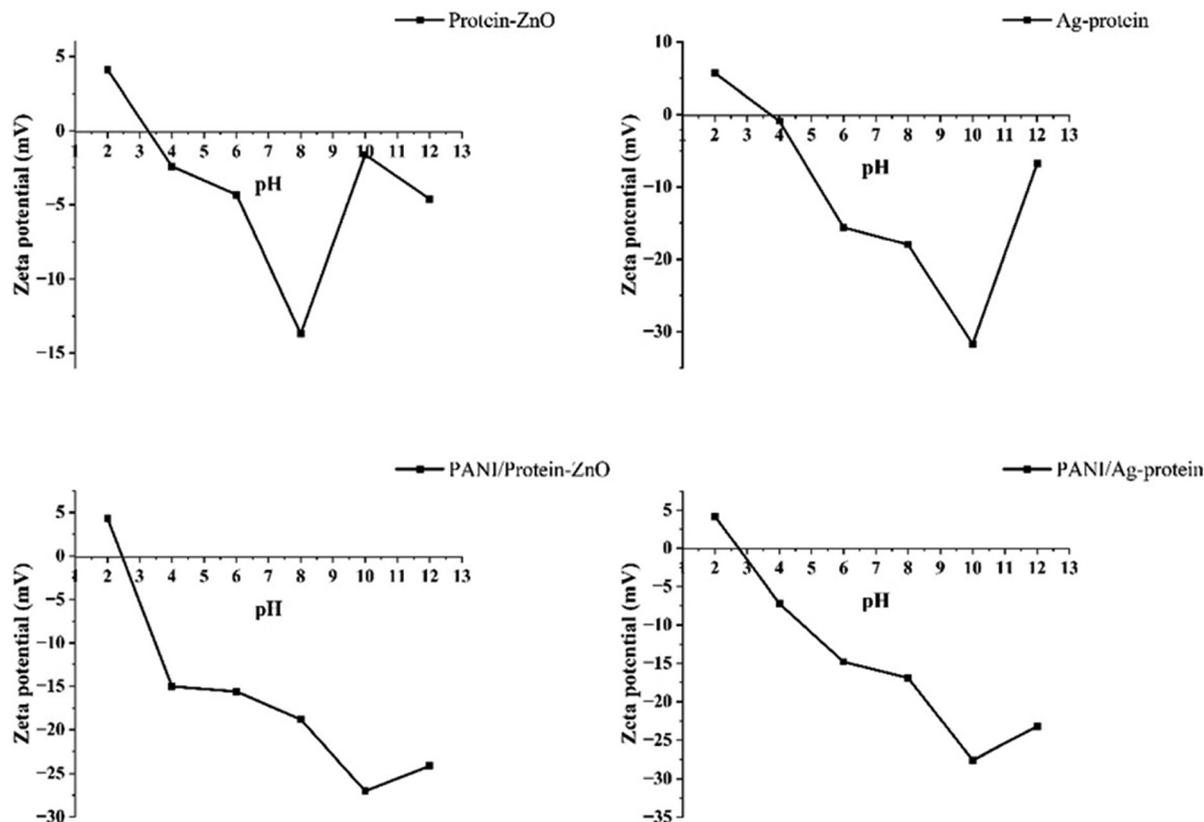
Fig. 6 Zeta potential values of the nanocomposites.

3.2. Cytotoxicity evaluation of composites

The cytotoxicity profiles of the synthesized nanocomposites were evaluated using a standard cell viability assay, and the results are depicted in Fig. 7. Both protein–ZnO (Fig. 7b) and Ag–protein (Fig. 7c) composites demonstrated excellent biocompatibility, with cell viability consistently exceeding 95% after 24 and 48 hours of incubation. These findings suggest that the incorporation of ZnO and Ag nanoparticles within the protein matrix does not elicit any significant cytotoxic response under the tested conditions, thereby affirming their suitability for biomedical and packaging applications. In contrast, the PANI-functionalized composites, namely PANI/protein–ZnO (Fig. 7d) and PANI/Ag–protein (Fig. 7e), exhibited moderately reduced cell viability, with approximately 80% of cells remaining viable at both time points. Although this level of viability still falls within an acceptable range for certain applications, the slight decrease may be attributed to the intrinsic oxidative properties or surface charge characteristics of polyaniline, which could influence cellular interactions. Further investigation into the dose-dependent effects and long-term biocompatibility of PANI-containing systems is warranted to fully elucidate their safety profile.

Fig. S8 illustrates the cytotoxicity assessment of the synthesized protein-based composites by determining their median lethal dose (LD_{50}) values and corresponding cell survival viability. The LD_{50} of the protein–ZnO composite was found to exceed 1 mg mL^{-1}, with a survival viability of 72.07%, suggesting

relatively low toxicity at the tested concentration. In comparison, the Ag–protein composite exhibited an LD_{50} of 1 mg mL^{-1} with a viability of 72.87%, while the PANI/protein–ZnO and PANI/Ag–protein composites demonstrated lower LD_{50} values of 0.76 mg mL^{-1} and 0.507 mg mL^{-1}, with survival viabilities of 40.05% and 34.79%, respectively. The native protein control showed an LD_{50} of 1 mg mL^{-1} and a viability of 69.83%. Notably, except for the PANI/Ag–protein composite, all tested materials maintained cell viability above 40% at their respective LD_{50} concentrations. This observation suggests that most composites do not exhibit pronounced cytotoxicity at the limit concentration, whereas the PANI/Ag–protein composite demonstrates comparatively higher toxicity, potentially due to synergistic effects between polyaniline and silver nanoparticles.

3.3. Minimum inhibitory concentration (MIC) assessment of nanocomposites

The minimum inhibitory concentration (MIC) is defined as the lowest concentration of an antimicrobial agent required to inhibit the visible growth of microorganisms under *in vitro* conditions. In this study, the MIC values of the synthesized nanocomposites were evaluated against two bacterial strains: *Bacillus cereus* (Gram-positive) and *Escherichia coli* (Gram-negative), as presented in Tables 3 and 4, respectively.

Following incubation, the turbidity of each test tube was visually compared with two controls: one containing nutrient
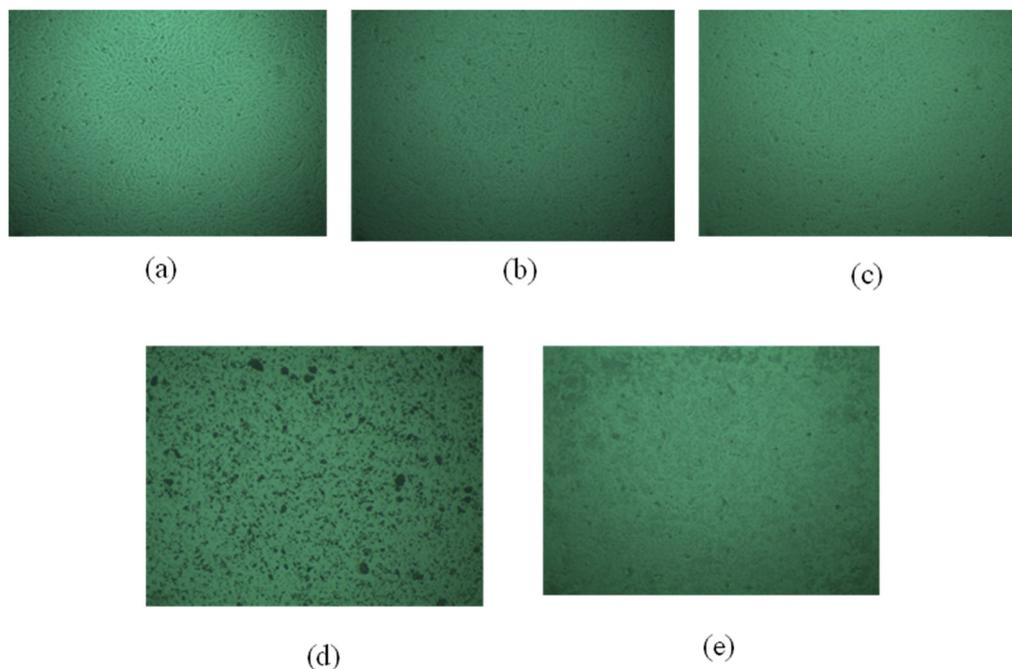
Fig. 7 *In vitro* cell cytotoxicity evaluation of (a) control, (b) protein–ZnO, (c) Ag–protein, (d) PANI/protein–ZnO, and (e) PANI/Ag–protein.

Table 3 (MIC), turbidity for different concentrations of nanocomposites after 24 h against *B. cereus*

Dilution of nanocomposites	5 mg mL^{-1} 0.5%	2.5 mg mL^{-1} 0.25%	1.25 mg mL^{-1} 0.12%	0.625 mg mL^{-1} 0.06%	0.325 mg mL^{-1} 0.03%	0.156 mg mL^{-1} 0.01%
Protein–ZnO	−	−	−	−	−	+
Ag–protein	−	−	−	−	+	+
PANI/protein–ZnO	−	−	−	−	+	+
PANI/Ag–protein	−	−	−	−	+	+

Positive (+): turbidity indicating growth; negative (−): no turbidity indicating the absence of growth.

Table 4 (MIC), turbidity for different concentrations of nanocomposites after 24 h against *E. coli*

Dilution of nanocomposites	5 mg mL^{-1} 0.5%	2.5 mg mL^{-1} 0.25%	1.25 mg mL^{-1} 0.12%	0.625 mg mL^{-1} 0.06%	0.325 mg mL^{-1} 0.03%	0.156 mg mL^{-1} 0.01%
Protein–ZnO	−	−	−	+	+	+
Ag–protein	−	−	−	−	+	+
PANI/protein–ZnO	−	−	−	−	+	+
PANI/Ag–protein	−	−	−	−	+	+

Positive (+): turbidity indicating growth; negative (−): no turbidity indicating the absence of growth.

broth without bacterial inoculation, and another serving as the untreated bacterial control. Any turbidity attributable to the nanocomposite itself was disregarded to ensure accurate interpretation. The MIC was determined as the concentration at which no visible bacterial growth was observed, indicating complete inhibition of microbial proliferation.

The protein–ZnO nanocomposite exhibited MIC values of 0.325 mg mL^{-1} against *B. cereus* and 1.25 mg mL^{-1} against *E. coli*, demonstrating higher efficacy against the Gram-positive strain. In contrast, the Ag–protein, PANI/protein–ZnO, and PANI/Ag–protein composites each exhibited an MIC value of 0.625 mg mL^{-1} against both bacterial strains, indicating

broad-spectrum antimicrobial activity. These findings are consistent with previous reports on the antimicrobial efficacy of silver nanoparticles, including their inhibitory effects against *Staphylococcus aureus*.[37]

The observed differences in MIC values may be attributed to variations in bacterial cell wall structure, nanoparticle composition, and the synergistic effects of the protein and polymer matrices. The enhanced activity of protein–ZnO against *B. cereus* highlights its potential as a selective antimicrobial agent, while the uniform MIC values of the other composites suggest their suitability for applications requiring broad-spectrum antibacterial coverage.

3.4. Finishing of leather with the nanocomposites

The synthesized nanocomposites were incorporated into the finishing formulation of leather, as illustrated in Fig. 8. Owing to their proteinaceous matrix, the composites functioned effectively as both fillers and binders, contributing to the structural integrity and adhesion of the finishing layer. Additionally, the presence of metal oxides such as ZnO and Ag endowed the formulation with antimicrobial properties, thereby enhancing the hygienic quality of the treated leather surface. Beyond their functional roles, the nanocomposites also imparted subtle coloration to the leather. Notably, the polyaniline (PANI)-based nanocomposites introduced two distinct shades of green, as evident in Fig. 8d and 8e. This chromatic contribution is attributed to the intrinsic color of PANI and its interaction with the protein–metal matrix, providing both aesthetic enhancement and functional benefits.

Furthermore, the treated leather samples demonstrated improved surface glazing and enhanced mechanical properties, including increased flexibility and abrasion resistance. These improvements suggest that the nanocomposite-based finishing formulations not only provide antimicrobial protection and visual appeal but also contribute to the durability and performance of the final leather product.

3.5. Antimicrobial activities of nanocomposites and coated finished leather

The antimicrobial efficacy of the synthesized nanocomposites was assessed using the agar well diffusion method in Petri dishes, with a protein solution serving as the control. The tests were conducted against two bacterial strains: *Bacillus cereus* (a Gram-positive bacterium) and *Escherichia coli* (a Gram-negative bacterium), with incubation periods ranging from 18 to 24 hours. The results are visually represented in Fig. 9, and the corresponding zones of inhibition are quantitatively reported in Table 5.

Zone of inhibition (ZOI) values for the four nanocomposite samples were compared with those of the positive (commercial antibiotic) and negative (protein, S-5) controls to evaluate antimicrobial activity, as shown in Fig. S4 and Table S7. For each, a two-tailed two-sample t-test was performed using Excel's T.TEST function. A significance threshold of $p < 0.05$ was used. All four samples showed statistically significantly larger ZOI compared to the negative control ($p < 0.05$), indicating effective antimicrobial activity for both *B. cereus* and *E. coli* bacteria. When compared to the positive control, all the samples showed a significant difference ($p < 0.05$), suggesting a slightly weaker efficacy compared to the commercial antibiotic for *B. cereus and E. coli*. However, the Ag–protein sample had a p-value greater than 0.05 for *E. coli*, which is statistically not significant, indicating that it has a similar effect to commercial antibiotics.

The antimicrobial mechanisms of the constituent nanoparticles are well-documented. Zinc oxide (ZnO) nanoparticles exert bactericidal effects by disrupting bacterial cell membranes, reducing cell surface hydrophobicity, and inhibiting
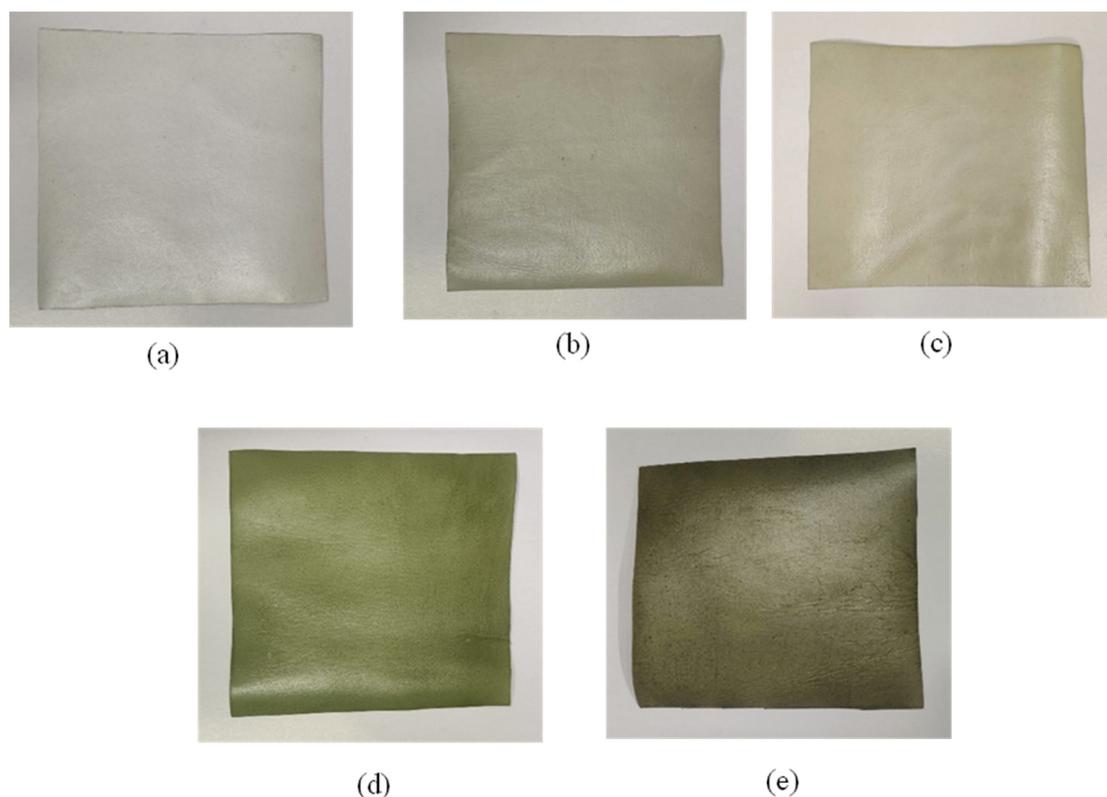

Fig. 8 Nanocomposite coated leather samples: (a) conventional (no nanocomposite was used), (b) protein–ZnO, (c) Ag–protein, (d) PANI/Ag–protein, and (e) PANI/protein–ZnO.
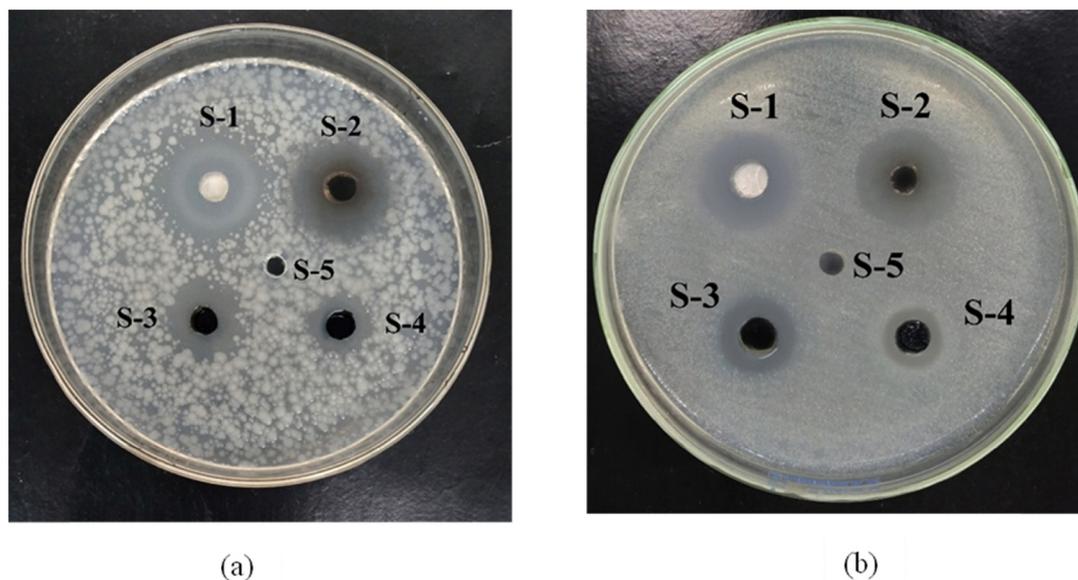
Fig. 9 Antimicrobial activity of protein–ZnO (S-1), Ag–protein (S-2), PANI/protein–ZnO (S-3), PANI/Ag–protein (S-4), and protein (S-5) against (a) *B. cereus* and (b) *E. coli*.

Table 5 Zone of inhibition of protein and the nanocomposites against *B. cereus* and *E. coli*

Bacteria	Protein–ZnO (S-1)	Ag–protein (S-2)	PANI/protein–ZnO (S-3)	PANI/Ag-Protein (S-4)	Control (Protein) (S-5)
B. cereus zone of inhibition (mm)	20 ± 0.70	18 ± 1	15 ± 1	13 ± 1	0
E. coli zone of inhibition (mm)	18 ± 1	22 ± 0.50	12 ± 0.50	12 ± 1	0

the transcription of genes responsible for oxidative stress resistance. ZnO also enhances intracellular bacterial elimination by stimulating the production of reactive oxygen species (ROS), which interact with vital cellular components such as proteins, lipids, and DNA, ultimately inducing apoptosis.[70]

Silver nanoparticles (AgNPs), on the other hand, owe their antimicrobial properties primarily to the release of silver ions and their high surface area-to-volume ratio.[71] These ions attach to essential bacterial structures, particularly thiol (–SH) groups, thereby compromising cellular integrity.[72] Additionally, AgNPs generate ROS and free radicals that damage the bacterial cell wall and interfere with respiratory enzymes, leading to impaired DNA replication and cell death.[73]

Polyaniline (PANI), a conductive polymer, also contributes to antimicrobial activity, which is influenced by its molecular weight. PANI synthesized *via* chemical oxidative polymerization using ammonium persulfate typically has a molecular weight below 100 kDa,[74] enabling it to penetrate bacterial cells and interact with intracellular biomolecules. The NH_3^+ and $–C_6H_5$ moieties of PANI bind to bacterial membranes through electrostatic and hydrophobic interactions, respectively. These interactions disrupt membrane integrity, induce cell lysis, and facilitate ROS-mediated damage to proteins and lipids.

As shown in Fig. 9, the protein control (S-5) exhibited negligible antibacterial activity, confirming its role as a stabilizing agent rather than an active antimicrobial component.

However, all four nanocomposite formulations demonstrated measurable zones of inhibition against both bacterial strains. The protein matrix played a crucial role in stabilizing the nanoparticles, preventing aggregation and potentially enhancing their interaction with microbial cells by modifying surface characteristics.

Among the tested formulations, protein–ZnO and Ag–protein nanocomposites exhibited superior antimicrobial activity against both *B. cereus* and *E. coli*, indicating effective nanoparticle stabilization and bioavailability. In contrast, the PANI-containing composites PANI/protein–ZnO and PANI/Ag–protein showed comparatively reduced antimicrobial efficacy, possibly due to altered nanoparticle surface properties that may hinder ROS generation or ion release.

Interestingly, both PANI-based composites demonstrated stronger antibacterial effects against *B. cereus*, with zones of inhibition of 15 mm and 13 mm, respectively. Their efficacy against *E. coli* was slightly diminished, with inhibition zones of 12 mm. This differential activity may reflect the inherent structural differences between Gram-positive and Gram-negative bacteria, as well as the complex interactions between PANI and the embedded nanoparticles.

The antibacterial efficacy of leather samples coated with various nanocomposite formulations was evaluated against *Bacillus cereus* (a Gram-positive bacterium) and *Escherichia coli* (a Gram-negative bacterium), as illustrated in Fig. 10 and
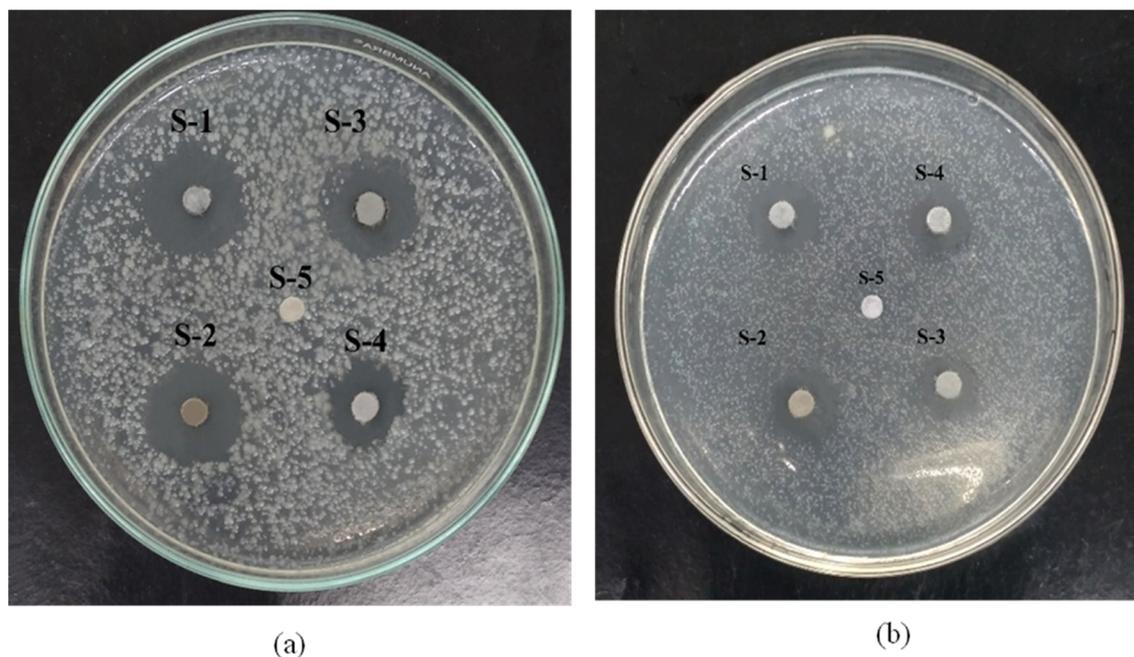
Fig. 10 Zone of inhibition (ZOI) of the leather samples finished by protein–ZnO (S-1), Ag–protein (S-2), PANI/protein–ZnO (S-3), PANI/Ag–protein (S-4), and conventional finishing (S-5, control-conventional finished leather) against (a) *B. cereus* and (b) *E. coli*.

Table 6 Zone of inhibition of the leather samples against *B. cereus* and *E. coli*

Bacteria		Protein–ZnO (S-1)	Ag–protein (S-2)	PANI/protein–ZnO (S-3)	PANI/Ag–protein (S-4)	Control (S-5)
B. cereus (zone of inhibition (mm))	Abrasion/rubbed leather	18 ± 2	20 ± 2	16 ± 2	13 ± 1	–
		8 ± 0.70	10 ± 0.50	6 ± 0.40	4 ± 0.80	–
E. coli (zone of inhibition (mm))	Abrasion/rubbed leather	12 ± 2	14 ± 1	12 ± 0.5	10 ± 1	–
		10 ± 1	12 ± 1	8 ± 0.80	7 ± 0.60	–

*Here, (–) indicates that no zone of inhibition was obtained for the sample control (S-5).

Fig. S9 and summarized in Table 6. The tested samples included: S-1 (protein–ZnO), S-2 (Ag–protein), S-3 (PANI/protein–ZnO), S-4 (PANI/Ag–protein), and S-5 (conventional aniline finish).

The control sample (S-5), coated with a conventional aniline-based finish, exhibited no observable antibacterial activity against either bacterial strain, confirming the absence of inherent antimicrobial properties in traditional leather finishing agents. In contrast, all nanocomposite-treated samples demonstrated measurable zones of inhibition, indicating effective antibacterial performance.

Among the tested formulations, S-2 (Ag–protein) showed the highest zone of inhibition against *B. cereus*, followed by S-1 (protein–ZnO), suggesting that silver-based nanocomposites possess superior bactericidal properties against Gram-positive bacteria. The PANI-incorporated samples (S-3 and S-4) exhibited comparatively lower antibacterial efficacy, consistent with previous observations regarding the interaction of PANI with nanoparticles and its potential influence on antimicrobial mechanisms.

The Gram-negative strain *E. coli* exhibited greater resistance to the nanocomposite treatments than *B. cereus*. This can be

attributed to the structural complexity of the *E. coli* cell envelope, which comprises a thin peptidoglycan layer surrounded by an outer membrane rich in lipoproteins, lipopolysaccharides, and phospholipids. This multilayered barrier reduces permeability and limits the penetration of reactive oxygen species (ROS) and metal ions, thereby diminishing the antimicrobial efficacy of surface treatments.[75]

Overall, the results indicate that nanocomposite-coated leather samples are more effective against Gram-positive bacteria, with Ag–protein and protein–ZnO formulations showing the most promising antibacterial performance. These findings support the potential applications of such nanocomposites in functional leather finishing, particularly for products requiring enhanced hygienic properties.

To validate the proposed mechanism underlying the release of Zn^{2+} and Ag^+ ions, the antimicrobial activity of synthetically prepared solutions of Zn^{2+} and Ag^+ at concentrations equivalent to 1 M, comparable to those present in the nanocomposite suspensions employed for zone of inhibition (ZOI) assays, was examined (Fig. S6). The Zn^{2+} solution produced nearly identical inhibitory effects against the Gram-positive strain *Bacillus cereus*,

with ZOI values ranging from 15 to 20 mm. Similarly, for the Gram-negative strain *Escherichia coli*, the Ag$^+$ solution demonstrated comparable antimicrobial performance, yielding ZOI values in the range of 20 to 25 mm. These findings confirm that the observed antibacterial activity in the nanocomposite suspensions can be attributed, at least in part, to the release of Zn^{2+} and Ag$^+$ ions.

It is well known that zinc and silver ions, which produce reactive oxidative stress (ROS) that includes superoxide anions (O^{2-}), hydroxyl radicals (–OH), and hydrogen peroxide (H$_2$O$_2$), are formed in aqueous solutions. To test this hypothesis, the effects of scavengers on bacterial death induced by reactive oxygen species were investigated by using the antioxidant ascorbic acid (AA). *B. cereus* and *E. coli* were grown in four separate agar plates, and a well was created (hole) on the plates by using the upper side of the micropipette tips. 10 µL of AA (5 mM) solution + 10 µL of nanocomposite (0.5 M) solution samples were applied into the holes created by micropipette tips. One hole is kept for control using only ascorbic acid. Similarly, the nanocomposite (without AA) at the same concentration and amount was applied to the other two plates. One hole is kept for control using only protein. The plates were kept in the incubator for 24 hours and the ZOI was measured and the diameter of the ZOI (with AA and without AA) was compared. The bacteria's survival is shown in Fig. S7. It is clearly observed that the presence of AA, a scavenger of ROS, was neutralized, and no bacterial death occurred. On the other hand, without AA bacteria, death was certain. Thus, it can be concluded that the hydroxyl radicals and hydrogen peroxide produced by metal–protein nanocomposites play a role in the process of killing bacteria.

3.6. Mechanical properties of nanocomposite coated finished leather

3.6.1. Colour fastness.
The fastness properties of the finished leather samples to rubbing were assessed under both dry and wet conditions, with the results presented in Tables S2 and S3. The evaluation was conducted using the standardized grey scale rating method, which is widely employed in color fastness testing to quantify the extent of color change and staining resulting from mechanical action. The grey scale provides a visual reference for assigning numerical ratings ranging from 1 to 5, where a rating of 5 indicates excellent fastness with negligible color change or staining, and a rating of 1 denotes poor fastness with pronounced deterioration. This method ensures consistent and objective assessment across different observers and testing conditions. All tested leather samples exhibited grey scale ratings between 3 and 5 for both dry and wet rub fastness, signifying satisfactory performance. Specifically, ratings of 4–5 were observed in most cases, indicating minimal color transfer and strong resistance to abrasion. These results suggest that the nanocomposite-based finishing formulations confer robust mechanical durability and color retention under typical usage conditions.

The observed fastness properties affirm the suitability of the developed finishes for practical applications where repeated handling and exposure to moisture are expected. Moreover, the consistent performance across both dry and wet conditions underscores the stability of the nanocomposite coatings and their potential for commercial leather finishing.

3.6.2. Heat fastness.
The heat fastness of the finished leather samples was evaluated using the grey scale rating method, with the results summarized in Table S4. This assessment measures the extent of color change or degradation that occurs when the leather is exposed to elevated temperatures, simulating conditions encountered during storage, transportation, or end-use in warm environments. Grey scale ratings, ranging from 1 (poor) to 5 (excellent), provide a standardized visual metric for quantifying thermal stability in terms of color retention. All nanocomposite-treated leather samples demonstrated ratings that met or exceeded the acceptable industry standards, indicating satisfactory resistance to heat-induced discoloration or surface deterioration. Compared to the control sample, which was finished using a conventional aniline-based formulation, the nanocomposite-coated samples exhibited comparable or superior thermal stability. This suggests that incorporating functional nanomaterials into the finishing matrix does not compromise the heat fastness of the leather and may even enhance it. These findings reinforce the suitability of the developed nanocomposite finishes for applications requiring thermal resilience and further support their potential for commercial adoption in high-performance leather products.

3.6.3. Water vapour permeability.
Water vapor and air permeability are critical parameters in determining the hygienic and physiological suitability of leather for wear. These properties directly influence essential functional attributes such as breathability and comfort, which are particularly important in the manufacturing of garments and footwear. Table S5 presents the water vapor permeability results of the finished leather samples. Among the tested formulations, the conventional aniline-finished leather (Sample-5) exhibited the lowest water vapor permeability. This outcome is consistent with expectations, as conventional finishing formulations typically involve the extensive use of chemical binders and pigments that form a dense, nonporous surface layer. Such coatings act as effective barriers to moisture transmission, thereby significantly reducing permeability. As reported by Milašienė *et al.*,[76] the decline in water vapor permeability is influenced by several factors, including reduced porosity of the upper layer, increased coating thickness, and the quantity of binder and pigment used in the formulation. In contrast, the experimental nanocomposite-based finishes demonstrated enhanced water vapor permeability. This improvement can be attributed to the reduced chemical load and the incorporation of porous nanostructures, which promote moisture diffusion through the leather matrix. The increased permeability observed in the experimental samples meets the required standards for breathable leather, suggesting a superior level of wearer comfort compared to traditionally finished leather. These findings underscore the potential of nanocomposite formulations to enhance the functional performance of leather without compromising its aesthetic or mechanical integrity.

3.6.4. Bond strength. Bond strength between the leather surface and the applied finish film is a critical parameter that reflects the adhesion, flexibility, and mechanical integrity of the finishing system. This property directly influences the durability and performance of the finished leather under mechanical stress, bending, and wear conditions. The bond strength is quantitatively assessed through standardized testing methods, which measure the force required to separate the finish film from the leather substrate. The results of this evaluation for all finished leather samples are presented in Table S6. The adhesion performance is influenced by several formulation factors, including the type and concentration of polymers, additives, and solvents used in the finishing matrix. These components govern the film-forming behavior and its interaction with the fibrous structure of the leather surface.

All tested samples met or exceeded the minimum bond strength requirements, indicating satisfactory adhesion across the formulations, Notably, samples S-1 through S-4, which incorporated nanocomposite finishes with reduced binder content compared to the conventional formulation (Sample-5), still demonstrated robust adhesion and mechanical strength. This suggests that, despite their lower binder concentrations, nanocomposite systems effectively anchor to the leather surface, likely due to enhanced interfacial interactions facilitated by the nanoscale components.

These findings affirm the structural integrity and practical viability of the experimental finishes, supporting their application in high-performance leather products where both aesthetic and mechanical properties are essential.

4. Conclusions

This study successfully developed and characterized four protein-based metal nanocomposites Protein–ZnO, Ag–protein, PANI/protein–ZnO, and PANI/Ag–protein for applications in functional leather finishing. These nanocomposites, synthesized by integrating proteins with metal nanoparticles, demonstrated promising antimicrobial efficacy and material performance, addressing the growing need for biofunctional coatings in leather processing. Comprehensive physicochemical characterization using UV-vis spectroscopy, FT-IR, XRD, zeta potential analysis, TGA, FESEM, and EDX confirmed the successful incorporation of ZnO and Ag nanoparticles within the protein and polyaniline matrices. The resulting nanocomposites exhibited particle sizes ranging from 32 to 45 nm and favorable surface charge profiles, contributing to their colloidal stability and bioactivity. Cytotoxicity assessments indicated that the formulations were non-toxic, supporting their potential for safe use in consumer products. Antimicrobial evaluations, including minimum inhibitory concentration (MIC) and zone of inhibition (ZOI) tests against *Bacillus cereus* and *Escherichia coli*, revealed significant antibacterial activity. Protein–ZnO showed the highest efficacy against *B. cereus* (ZOI = 20 mm), while Ag–protein was the most effective against *E. coli* (ZOI = 22 mm). When applied to leather substrates, the nanocomposite finishes enhance key performance attributes, including surface glaze, antimicrobial protection, and coloration. Notably, protein–ZnO-treated leather exhibited the highest ZOI (18 mm) against *B. cereus*, and Ag–protein-treated leather showed a ZOI of 14 mm against *E. coli*, outperforming conventional finishes. These findings demonstrate the potential of protein-based metal nanocomposites to improve the functional and aesthetic properties of low-grade crust leather while preserving its natural texture and appearance. The incorporation of bioactive nanoparticles offers a sustainable and effective approach to leather finishing, with implications for hygiene, durability, and consumer comfort. Future research may explore the electrical conductivity and electroactive behavior of polyaniline-based nanocomposites, paving the way for advanced applications in smart textiles, wearable electronics, and multifunctional leather products.

Author contributions

Abdulla-Al-Mamun M: conceptualization, methodology, writing – reviewing, supervision, and project administration; Liza SA: formal analysis, investigation, data curation, writing – original draft preparation, equal contribution of the first authorship; Nazmul Islam M: protein and amino acid analysis; Rezaul Karim Rana M: SDS-PAGE analysis; Shariful Islam M: supervision. All authors have read and agreed to the publication of the manuscript.

Conflicts of interest

There are no conflicts to declare.

Data availability

This manuscript contains all of the data generated or analyzed during this research. The data supporting this article have been included as part of the supplementary information (SI). Supplementary information is available. See DOI: https://doi.org/10.1039/d5ma01510c.

Acknowledgements

References

1 D. R. Bagal-Kestwal, R. M. Kestwal and B. H. Chiang, Bio-based Nanomaterials and Their Bionanocomposites, *Nanomaterials and Nanocomposites: Zero-to Three-Dimensional Materials and Their Composites*, Wiley-VCH Verlag GmbH & Co. KGaA, 2016, pp. 255–330, DOI: 10.1002/9783527683772.ch8.

2 H. Ahari, L. Golestan, S. A. A. Anvar, I. Cacciotti, F. Garavand, A. Rezaei, M. A. Sani and S. M. Jafari, Bio-nanocomposites as

food packaging materials; the main production techniques and analytical parameters, *Adv. Colloid Interface Sci.*, 2022, **310**, 102806, DOI: 10.1016/j.cis.2022.102806.

3 A. Rodzik, P. Pomastowski, G. N. Sagandykova and B. Buszewski, Interactions of whey proteins with metal ions, *Int. J. Mol. Sci.*, 2020, **21**(6), 2156, DOI: 10.3390/ijms21062156.

4 R. Javed, M. Zia, S. Naz, S. O. Aisida, N. U. Ain and Q. Ao, Role of capping agents in the application of nanoparticles in biomedicine and environmental remediation: recent trends and future prospects, *J. Nanobiotechnol.*, 2020, **18**(1), 172, DOI: 10.1186/s12951-020-00704-4.

5 S. Gulati, M. Sachdeva and K. K. Bhasin, Capping agents in nanoparticle synthesis: Surfactant and solvent system, *AIP Conf. Proc.*, 2018, **1953**(1), 030214, DOI: 10.1063/1.5032549.

6 J. F. Floriano, M. C. da Silva, M. M. de Oliveira and A. A. de Souza, Metal-protein nanocomposites: A sustainable approach for antimicrobial applications in leather finishing, *J. Clean. Prod.*, 2023, **408**, 137245, DOI: 10.1016/j.jclepro.2023.137245.

7 W. Xiao, Z. Liu, W. Luo, Y. Gao, L. Chang, Y. Li and P. Xu, Specific and unbiased detection of polyubiquitination via a sensitive non-antibody approach, *Anal. Chem.*, 2020, **92**(1), 1074–1080, DOI: 10.1021/acs.analchem.9b04594.

8 R. Hu, Y. Li, Y. Yang and M. Liu, Mass spectrometry-based strategies for single-cell metabolomics, *Mass Spectrom. Rev.*, 2023, **42**(1), 67–94, DOI: 10.1002/mas.21689.

9 M. Darder, P. Aranda and E. Ruiz-Hitzky, Bionanocomposites: A New Concept of Ecological, Bioinspired, and Functional Hybrid Materials, *Adv. Mater.*, 2007, **19**, 1309–1319, DOI: 10.1002/adma.200602328.

10 S. C. Warangkar, M. R. Deshpande, N. D. Totewad and A. A. Singh, Antibacterial, Antifungal and Antiviral Nanocomposites: Recent Advances and Mechanisms of Action, *Biocomposites – Recent Advances*, IntechOpen, 2022, DOI: 10.5772/intechopen.108994.

11 A. Mobed, M. Hasanzadeh and F. Seidi, Anti-bacterial activity of gold nanocomposites as a new nanomaterial weapon to combat photogenic agents: recent advances and challenges, *RSC Adv.*, 2021, **11**, 34688–34698, DOI: 10.1039/D1RA06030A.

12 M. Harun-Ur-Rashid, T. Foyez, S. B. N. Krishna, S. Poda and A. B. Imran, Recent advances of silver nanoparticle-based polymer nanocomposites for biomedical applications, *RSC Adv.*, 2025, **15**, 8480–8505, DOI: 10.1039/D4RA08220F.

13 L. M. Ditu, R. Bucuresteanu, M. Ionita, A. Neacsu and I. Calinescu, Antimicrobial and Antibiofilm Properties of Nanocomposite Surfaces with Biomedical Applications, *Nanocomposites – Properties, Preparations and Applications*, IntechOpen, 2024, DOI: 10.5772/intechopen.115120.

14 M. Gargano, A. Bacardit, G. Sannia and V. Lettera, From Leather Wastes back to Leather Manufacturing: The Development of New Bio-Based Finishing Systems, *Coatings*, 2023, **13**(4), 775, DOI: 10.3390/coatings13040775.

15 C. Winter, C. Borges Agustini and M. Gutterres, Behavior of Polymer Films and its Blends for Leather Finishing, *Trends Text. Eng. Fashion Technol.*, 2018, **1**(4), 93–102, DOI: 10.31031/TTEFT.2018.01.000518.

16 X. Wu, J. Wu, C. Mu, C. Wang and W. Lin, Advances in antimicrobial polymer coatings in the leather industry: a comprehensive review, *Ind. Eng. Chem. Res.*, 2021, **60**(42), 15004–15018, DOI: 10.1021/acs.iecr.1c02600.

17 M. R. Khan, M. S. R. Shakil, B. Vorselaars, M. Rahman, I. A. Jawad and W. Ahmed, Nanotechnology in Leather Manufacturing, ed. Jackson, M. J., Ahmed, W., in *Micro and Nanomanufacturing*, Springer Nature, Switzerland, 2024, vol. 2, pp. 23–52, DOI: 10.1007/978-3-031-70499-4_2.

18 B. Sahu, A. Ramesh and F. Zameer, Impact of nanomaterials on leather: a nano-Saga from processing to application, *Clean Technol. Environ. Policy*, 2024, 1–28, DOI: 10.1007/s10098-024-02912-0.

19 T. S. Vijayakumar, S. Mahboob, G. Bupesh, S. Vasanth, K. A. Al-Ghanim, F. Al-Misned and M. Govindarajan, Facile synthesis and biophysical characterization of egg albumen-wrapped zinc oxide nanoparticles: a potential drug delivery vehicle for anticancer therapy, *J. Drug Delivery Sci. Technol.*, 2020, **60**, 102015, DOI: 10.1016/j.jddst.2020.102015.

20 A. M. Alahe, S. A. Liza, R. K. Raha and M. Abdulla-Al-Mamun, Protein-Based Polymeric Metal–Nanocomposite Derived From Egg Albumin: A Highly Effective Antimicrobial Agent Against Bacteria, *Appl. Organomet. Chem.*, 2025, **39**(1), e7780, DOI: 10.1002/aoc.7780.

21 Y. A. Arfat, S. Benjakul, T. Prodpran, P. Sumpavapol and P. Songtipya, Properties and antimicrobial activity of fish protein isolate/fish skin gelatin film containing basil leaf essential oil and zinc oxide nanoparticles, *Food Hydrocoll.*, 2014, **41**, 265–273, DOI: 10.1016/j.foodhyd.2014.04.023.

22 M. Sitohy, A. R. Al-Mohammadi, A. Osman, S. Abdel-Shafi, N. El-Gazzar, S. Hamdi, S. H. Ismail and G. Enan, Silver-protein nanocomposites as antimicrobial agents, *Nanomaterials*, 2021, **11**(11), 3006, DOI: 10.3390/nano11113006.

23 A. Amani, M. Montazer and M. Mahmoudirad, Synthesis of applicable hydrogel corn silk/ZnO nanocomposites on polyester fabric with antimicrobial properties and low cytotoxicity, *Int. J. Biol. Macromol.*, 2019, **123**, 1079–1090, DOI: 10.1016/j.ijbiomac.2018.11.093.

24 G. J. C. Canama, M. C. L. Delco, R. A. Talandron and N. P. Tan, Synthesis of chitosan-silver nanocomposite and its evaluation as an antibacterial coating for mobile phone glass protectors, *ACS Omega*, 2023, **8**(20), 17699–17711, DOI: 10.1021/acsomega.3c00191.

25 Y. Xiao, Y. Liu, S. Kang, K. Wang and H. Xu, Development and evaluation of soy protein isolate-based antibacterial nanocomposite films containing cellulose nanocrystals and zinc oxide nanoparticles, *Food Hydrocoll.*, 2020, **106**, 105898, DOI: 10.1016/j.foodhyd.2020.105898.

26 E. Yuan, M. Zhou, S. Nie and J. Ren, Interaction mechanism between ZnO nanoparticles-whey protein and its effect on toxicity in GES-1 cells, *J. Food Sci.*, 2022, **87**(6), 2417–2426, DOI: 10.1111/1750-3841.16193.

27 N. Strambeanu, L. Demetrovici, D. Dragos and M. Lungu, Nanoparticles: Definition, classification and general physical properties. in *Nanoparticles' Promises and Risks: Characterization, Manipulation, and Potential Hazards to Humanity and the*

Environment, Springer International Publishing, Cham, 2014, pp. 3–8, DOI: 10.1007/978-3-319-11728-7_1.

28 C. Gaidau, A. Petica, M. Ignat, O. Iordache, L. M. Ditu and M. Ionescu, Enhanced photocatalysts based on Ag-TiO2 and Ag-N-TiO2 nanoparticles for multifunctional leather surface coating, *Open Chem.*, 2016, **14**(1), 383–392, DOI: 10.1515/chem-2016-0040.

29 J. Liu, J. Ma, Y. Bao, J. Wang, H. Tang and L. Zhang, Poly-acrylate/surface-modified ZnO nanocomposite as film-forming agent for leather finishing, *Int. J. Polym. Mater. Polym.*, 2014, **63**(16), 809–814, DOI: 10.1080/00914037.2014.886217.

30 W. Chen, L. Feng and B. Qu, In situ synthesis of poly (methyl methacrylate)/MgAl layered double hydroxide nano-composite with high transparency and enhanced thermal properties, *Solid State Commun.*, 2004, **130**(3–4), 259–263, DOI: 10.1016/j.ssc.2004.01.031.

31 Y. Wang, J. Ma, Q. Xu and J. Zhang, Fabrication of anti-bacterial casein-based ZnO nanocomposite for flexible coat-ings, *Mater. Des.*, 2017, **113**, 240–245, DOI: 10.1016/j.matdes.2016.09.082.

32 S. Saravanabhavan, K. J. Sreeram, J. Raghava Rao and B. Unni Nair, The three pot solution for chromium, tannins and solid wastes: Recovery and reuse technique for spent semi-chrome liquor and chrome shavings, *J. Soc. Leather Technol. Chem.*, 2004, **88**(5), 202–207.

33 S. A. Liza and M. Abdulla-Al-Mamun, Microbial degradation of tannery chrome-solid waste using Bacillus thuringiensis: optimization of collagen hydrolysate extraction via response surface methodology, *RSC Sustainability*, 2025, **3**, 3198–3214, DOI: 10.1039/D4SU00666F.

34 K. E. Ramohlola, G. R. Monana, M. J. Hato, K. D. Modibane, K. M. Molapo, M. Masikini, S. B. Mduli and E. I. Iwuoha, Polyaniline-metal organic framework nanocomposite as an efficient electrocatalyst for hydrogen evolution reaction, *Composites, Part B*, 2018, **137**, 129–139, DOI: 10.1016/j.compositesb.2017.11.016.

35 H. K. Mahre, L. Dalheim, G. K. Edvinsen, E. O. Elvevoll and I. J. Jensen, Protein Determination_Method Matters, *Foods*, 2018, **7**(1), 5, DOI: 10.3390/foods7010005.

36 P. Weber, Determination of amino acids in food and feed by microwave hydrolysis and UHPLC-MS/MS, *J. Chromatogr. B:Anal. Technol. Biomed. Life Sci.*, 2022, **1209**, 123429, DOI: 10.1016/j.jchromb.2022.123429.

37 P. Parvekar, J. Palaskar, S. Metgud, R. Maria and S. Dutta, The minimum inhibitory concentration (MIC) and mini-mum bactericidal concentration (MBC) of silver nano-particles against Staphylococcus aureus, *Biomater. Investig. Dent.*, 2020, **7**(1), 105–109, DOI: 10.1080/26415275.2020.1796674.

38 F. W. Sosulski and G. I. Imafidon, Amino acid composition and nitrogen-to-protein conversion factors for animal and plant foods, *J. Agric. Food Chem.*, 1990, **38**(6), 1351–1356, DOI: 10.1021/jf00096a011.

39 M. Arnold and A. Barbul, Nutrition and wound healing, *Plast. Reconstr. Surg.*, 2006, **117**(7S), 42S–58S, DOI: 10.1097/01.prs.0000225432.17501.6c.

40 D. Acharya, B. Mohanta, P. Pandey, M. Singha and F. Nasiri, Optical and antibacterial properties of synthesised silver nanoparticles, *Micro Nano Lett.*, 2017, **12**(4), 223–226, DOI: 10.1049/mnl.2016.0666.

41 R. Das and S. Sarkar, Optical properties of silver nano-cubes, *Opt. Mater.*, 2015, **48**, 203–208, DOI: 10.1016/j.optmat.2015.07.038.

42 D. K. Singh, D. K. Pandey, R. R. Yadav and D. Singh, A study of nanosized zinc oxide and its nanofluid, *Pramana*, 2012, **78**(5), 759–766, DOI: 10.1007/s12043-012-0275-8.

43 L. Shi, J. Zhou and S. Gunasekaran, Low temperature fabrication of ZnO–whey protein isolate nanocomposite, *Mater. Lett.*, 2008, **62**(28), 4383–4385, DOI: 10.1016/j.matlet.2008.07.038.

44 M. Venkatesham, D. Ayodhya, A. Madhusudhan, A. Santoshi Kumari, G. Veerabhadram and K. Girija Mangatayaru, A novel green synthesis of silver nanoparticles using gum karaya: characterization, antimicrobial and catalytic activity studies, *J. Clust. Sci.*, 2014, **25**(2), 409–422, DOI: 10.1007/s10876-013-0620-1.

45 M. V. Fuke, A. Vijayan, P. Kanitkar, M. Kulkarni, B. B. Kale and R. C. Aiyer, Ag-polyaniline nanocomposite cladded planar optical waveguide based humidity sensor, *J. Mater. Sci.: Mater. Electron.*, 2009, **20**(8), 695–703, DOI: 10.1007/s10854-008-9787-x.

46 M. S. Tamboli, M. V. Kulkarni, R. H. Patil, W. N. Gade, S. C. Navale and B. B. Kale, Nanowires of silver-polyaniline nanocomposite synthesized via in situ polymerization and its novel functionality as an antibacterial agent, *Colloids Surf., B*, 2012, **92**, 35–41, DOI: 10.1016/j.colsurfb.2011.11.006.

47 S. Krimm and J. Bandekar, Vibrational spectroscopy and conformation of peptides, polypeptides, and proteins, *Adv. Protein Chem.*, 1986, **38**, 181–364, DOI: 10.1016/S0065-3233(08)60528-8.

48 R. Murali, A. Anumary, M. Ashokkumar, P. Thanikaivelan and B. Chandrasekaran, Hybrid biodegradable films from collagenous wastes and natural polymers for biomedical applications, *Waste Biomass Valorization*, 2011, **2**(3), 323–335, DOI: 10.1007/s12649-011-9072-8.

49 D. Pradhan, L. B. Sukla, B. B. Mishra and N. Devi, Biosorp-tion for removal of hexavalent chromium using microalgae Scenedesmus sp, *J. Cleaner Prod.*, 2019, **209**, 617–629, DOI: 10.1016/j.jclepro.2018.10.288.

50 N. Jayarambabu, B. S. Kumari, K. V. Rao and Y. T. Prabhu, Germination and growth characteristics of mungbean seeds (Vigna radiata L.) affected by synthesized zinc oxide nanoparticles, *Int. J. Curr. Eng. Technol.*, 2014, **4**(5), 3411–3416.

51 J. Zhao, J. Wang and G. Ma, Extremely concentrated silver nanoparticles stabilized in aqueous solution by Bovine Serum Albumin (BSA), *Nano-Struct. Nano-Objects*, 2019, **19**, 100349, DOI: 10.1016/j.nanoso.2019.100349.

52 M. Ragothaman, A. K. Villalan, A. Dhanasekaran and T. Palanisamy, Bio-hybrid hydrogel comprising collagen-capped silver nanoparticles and melatonin for accelerated

tissue regeneration in skin defects, *Mater. Sci. Eng. C.*, 2021, **128**, 112328, DOI: 10.1016/j.msec.2021.112328.

53 Y. B. Wankhede, S. B. Kondawar, S. R. Thakare and P. S. More, Synthesis and characterization of silver nanoparticles embedded in polyaniline nanocomposite, *Adv. Mater. Lett.*, 2013, **4**(1), 89–93, DOI: 10.5185/amlett.2012.icnano.108.

54 K. R. Reddy, B. C. Sin, K. S. Ryu, J. C. Kim, H. Chung and Y. Lee, Conducting polymer functionalized multi-walled carbon nanotubes with noble metal nanoparticles: synthesis, morphological characteristics and electrical properties, *Synth. Met.*, 2009, **159**(7–8), 595–603, DOI: 10.1016/j.synthmet.2008.11.030.

55 S. Muthusamy and J. Charles, In situ synthesis and characterization of polyaniline/prussian blue/zinc oxide nanocomposite, *Polym. Bull.*, 2019, **76**(1), 119–137, DOI: 10.1007/s00289-018-2350-x.

56 M. Vanaja and G. Annadurai, Coleus aromaticus leaf extract mediated synthesis of silver nanoparticles and its bactericidal activity, *Appl. Nanosci.*, 2013, **3**(3), 217–223, DOI: 10.1007/s13204-012-0121-9.

57 Y. Li, Z. Li and F. Zheng, Polyaniline/silver/cerium nitrate ternary composite: Synthesis, characterization and enhanced electrochemical properties, *J. Appl. Polym. Sci.*, 2015, **132**(46), 42785, DOI: 10.1002/app.42785.

58 L. J. Pan, L. Pu, Y. Shi, T. Sun, R. Zhang and Y. O. Zheng, Hydrothermal synthesis of polyaniline mesostructures, *Adv. Funct. Mater.*, 2006, **16**(10), 1279–1288, DOI: 10.1002/adfm.200500543.

59 H. S. Abdulla and A. I. Abbo, Optical and electrical properties of thin films of polyaniline and polypyrrole, *Int. J. Electrochem. Sci.*, 2012, **7**(11), 10666–10678, DOI: 10.1016/S1452-3981(23)16893-3.

60 R. Paulraj, P. Shankar, G. K. Mani, L. Nallathambi and J. B. B. Rayappan, Fabrication of PANI-ZnO nanocomposite thin film for room temperature methanol sensor, *J. Mater. Sci.*, 2017, **28**(15), 10799–10805, DOI: 10.1007/s10854-017-6857-y.

61 S. Muthusamy and J. Charles, In situ synthesis and characterization of polyaniline/prussian blue/zinc oxide nanocomposite, *Polym. Bull.*, 2019, **76**(1), 119–137, DOI: 10.1007/s00289-018-2350-x.

62 R. Kumar, R. D. Anandjiwala and A. Kumar, Thermal and mechanical properties of mandelic acid-incorporated soy protein films, *J. Therm. Anal. Calorim.*, 2016, **123**(2), 1273–1279, DOI: 10.1007/s10973-015-5035-9.

63 J. A. Lee, M. J. Yoon, E. S. Lee, D. Y. Lim and K. Y. Kim, Preparation and characterization of cellulose nanofibers (CNFs) from microcrystalline cellulose (MCC) and CNF/poly amide 6 composites, *Macromol. Res.*, 2014, **22**(7), 738–745, DOI: 10.1007/s13233-014-2121-y.

64 M. O. Ansari and F. Mohammad, Thermal stability, electrical conductivity and ammonia sensing studies on p-toluenesulfonic acid doped polyaniline: titanium dioxide (pTSA/Pani: TiO2) nanocomposites, *Sens. Actuators, B*, 2011, **157**(1), 122–129, DOI: 10.1016/j.snb.2011.03.036.

65 J. G. Wang, Y. Yang, Z. H. Huang and F. Kang, Interfacial synthesis of mesoporous MnO$_2$/polyaniline hollow spheres and their application in electrochemical capacitors, *J. Power Sources*, 2012, **204**, 236–243, DOI: 10.1016/j.jpowsour.2011.12.057.

66 A. G. Kaningini, S. Azizi, N. Sintwa, K. Mokalane, K. C. Mohale, F. N. Mudau and M. Maaza, Effect of optimized precursor concentration, temperature, and doping on optical properties of ZnO nanoparticles synthesized via a green route using bush tea (Athrixia phylicoides DC.) leaf extracts, *ACS Omega*, 2022, **7**(36), 31658–31666, DOI: 10.1021/acsomega.2c00530.

67 A. R. Maheo, B. S. M. Vithiya, T. A. Arul Prasad, V. L. Mangesh, T. Perumal, W. H. Al-Qahtani and M. Govindasamy, Cytotoxic, antidiabetic, and antioxidant study of biogenically improvised elsholtzia blanda and chitosan-assisted zinc oxide nanoparticles, *ACS Omega*, 2023, **8**(12), 10954–10967, DOI: 10.1021/acsomega.2c07530.

68 J. D. Clogston and A. K. Patri, Zeta potential measurement, *Characterization of nanoparticles intended for drug delivery*, Humana press, Totowa, NJ, 2010, pp. 63–70, DOI: 10.1007/978-1-60327-198-1_6.

69 K. Cheng, W. Weng, H. Wang and S. Zhang, In vitro behavior of osteoblast-like cells on fluoridated hydroxyapatite coatings, *Bio. Mater.*, 2005, **26**(32), 6288–6295, DOI: 10.1016/j.biomaterials.2005.03.041.

70 Y. Xie, Y. He, P. L. Irwin, T. Jin and X. Shi, Antibacterial activity and mechanism of action of zinc oxide nanoparticles against Campylobacter jejuni, *Appl. Environ. Microbiol.*, 2011, **77**(7), 2325–2331, DOI: 10.1128/AEM.02149-10.

71 X. Chen and H. J. Schluesener, Nanosilver: a nanoproduct in medical application, *Toxicol. Lett.*, 2008, **176**(1), 1–12, DOI: 10.1016/j.toxlet.2007.10.004.

72 J. R. Morones, J. L. Elechiguerra, A. Camacho, K. Holt, J. B. Kouri, J. T. Ramírez and M. J. Yacaman, The bactericidal effect of silver nanoparticles, *Nanotechnology*, 2005, **16**(10), 2346, DOI: 10.1088/0957-4484/16/10/059.

73 Y. Y. Loo, Y. Rukayadi, M. A. R. Nor-Khaizura, C. H. Kuan, B. W. Chieng, M. Nishibuchi and S. Radu, In vitro antimicrobial activity of green synthesized silver nanoparticles against selected Gram-negative foodborne pathogens, *Front. Microbiol.*, 2018, **9**, 1555, DOI: 10.3389/fmicb.2018.01555.

74 H. S. Kolla, S. P. Surwade, X. Zhang, A. G. MacDiarmid and S. K. Manohar, Absolute molecular weight of polyaniline, *J. Am. Chem. Soc.*, 2005, **127**(48), 16770–16771, DOI: 10.1021/ja055327k.

75 F. Fu, L. Li, L. Liu, J. Cai, Y. Zhang, J. Zhou and L. Zhang, Construction of cellulose based ZnO nanocomposite films with antibacterial properties through one-step coagulation, *ACS Appl. Mater. Interfaces*, 2015, **7**(4), 2597–2606, DOI: 10.1021/am507639b.

76 D. Milašienė, V. Jankauskaitė and R. Arcišauskaitė, Prediction of stress relaxation in laminated leather layers, *Mater. Sci.*, 2003, **9**(1), 73–79.